nature communications

Article

https://doi.org/10.1038/s41467-025-61448-z

Androgen receptor promotes arachidonic acid metabolism and angiogenic microenvironment in AFP-negative hepatocellular carcinoma

Received: 2 August 2024

Accepted: 19 June 2025

Zhilong Lin[1,11], Xiaofei Liu[2,11], Houwei Wang[1,11], Shumin Li[3,11], Ziqiang Miao[4,11], Jing Yang[2], Yuting Zhang[5], Kai Lei[1], Yifan Wu[2], Youmei Kang[6], Ruoyin Zheng[1], Zonglin Xie[3], Yixi Wen[6], Xiaoxue Ren[3], Chunxiao Liu[6], Alfred Sze-Lok Cheng[7], Yubin Xie[6], Shuling Chen[6,8], Ming Kuang[1,6], Sui Peng[2,6,9,12] ✉, Zhenwei Peng[9,10,12] ✉ & Zihao Dai[1,12] ✉

Alpha-fetoprotein (AFP) is a classic biomarker for hepatocellular carcinoma (HCC). AFP-positive HCC (AFP$^+$ HCC) has been intensively investigated; however, the genomic, transcriptomic and microenvironmental characteristics of AFP-negative HCC (AFP$^-$ HCC) remain to be deciphered. Here we show that tumors display mild differences in genetic alterations between AFP$^-$ HCC and AFP$^+$ HCC patients, while AFP$^-$ HCC exhibits hyperactive arachidonic acid metabolism. Furthermore, the transcription activity of androgen receptor (AR) is significantly increased in AFP$^-$ HCC and plays a positive regulatory role in arachidonic acid metabolism and its metabolite 11,12-epoxyeicosatrienoic acid (11,12-EET). The tumor-derived 11,12-EET exhibits high affinity for EGFR that promotes the migration and tube formation of endothelial cells in vitro. Combination of lenvatinib and bicalutamide (an AR antagonist) enhances the therapeutic efficacy for AFP$^-$ HCC. Overall, we uncover the AR-mediated hyperactive arachidonic acid metabolism in AFP$^-$ HCC, and reveal AR-11,12-EET-EGFR axis-induced angiogenesis, providing a promising strategy of combined AR antagonist with lenvatinib for AFP$^-$ HCC treatment.

Liver cancer is the third leading cause of cancer-related deaths, with an overall low 5-year survival rate of 20.8%[1,2]. Hepatocellular carcinoma (HCC) accounts for 80–90% of liver cancer worldwide[3]. Alpha-fetoprotein (AFP) is the most widely used biomarker for HCC in clinical practice, primarily aiding in HCC screening, diagnosis, prognosis prediction, and treatment efficacy monitoring[4]. However, our knowledge on genetic features, molecular characteristics and tumor ecosystem profiling of AFP-related HCCs is very limited.

---

[1]Center of Hepato-Pancreato-Biliary Surgery, The First Affiliated Hospital of Sun Yat-sen University, Guangzhou, China. [2]Department of Gastroenterology and Hepatology, the First Affiliated Hospital, Sun Yat-sen University, Guangzhou, China. [3]Department of Oncology, The First Affiliated Hospital, Sun Yat-sen University, Guangzhou, China. [4]Organ Transplant Center, The First Affiliated Hospital, Sun Yat-sen University, Guangzhou, China. [5]Department of Pathology, The First Affiliated Hospital, Sun Yat-sen University, Guangzhou, China. [6]Institute of Precision Medicine, The First Affiliated Hospital, Sun Yat-sen University, Guangzhou, China. [7]School of Biomedical Sciences, The Chinese University of Hong Kong, Hong Kong, China. [8]Institute of Diagnostic and Interventional Ultrasound, The First Affiliated Hospital, Sun Yat-sen University, Guangzhou, China. [9]Clinical Trials Unit, The First Affiliated Hospital, Sun Yat-sen University, Guangzhou, China. [10]Cancer Center, The First Affiliated Hospital of Sun Yat-sen University, Guangzhou, China. [11]These authors contributed equally: Zhilong Lin, Xiaofei Liu, Houwei Wang, Shumin Li, Ziqiang Miao. [12]These authors jointly supervised this work: Sui Peng, Zhenwei Peng, Zihao Dai.
✉e-mail: pengsui@mail.sysu.edu.cn; pzhenw@mail.sysu.edu.cn; daizihao@mail2.sysu.edu.cn

Extensive evidence has established that AFP exerts dual oncogenic effects by enhancing tumor cell proliferation and suppressing apoptosis in HCC[5]. In addition, AFP also plays pivotal roles in regulating immune responses, for instance, it can induce natural killer (NK) cell apoptosis, promote Treg differentiation and inhibit dendritic cell (DC) maturation, ultimately repressing CD8$^+$ T cells and resulting in an immunosuppressive microenvironment[6]. Recently, comprehensive multi-omics approaches integrating whole-exome sequencing (WES), bulk RNA-sequencing (RNA-seq) and single-cell RNA-sequencing (scRNA-seq) have been adopted to reveal the multi-dimensional characteristics of tumor immune ecosystem in AFP-positive HCC (AFP$^+$ HCC, serum AFP level ≥ 20 ng/mL at diagnosis). The findings showed that tumor-associated macrophages (TAMs) suppressed CD8$^+$ T cell function through the SPP1-CD44 axis in the tumor microenvironment (TME) of AFP$^+$ HCC, thus providing a promising target for achieving a more favorable efficacy in AFP$^+$ HCC treatment[7]. Therefore, AFP$^+$ HCC has been widely explored in previous studies[6–10].

However, approximately 30–40% of HCC showed negative AFP serum level (AFP$^-$ HCC, serum AFP level < 20 ng/mL at diagnosis)[11,12]. Of note, several recent global clinical trials have indicated that AFP$^-$ HCC patients showed moderate treatment response to the first-line drug lenvatinib or its analogues[13–15]. Nevertheless, due to the few studies on AFP$^-$ HCC, the underlying mechanism remains largely unknown without available interventions. Therefore, we aimed to comprehensively decipher the genomic, transcriptomic and microenvironmental characteristics of AFP$^-$ HCC that helped guide the precise treatment strategy for this subtype of HCC.

In the present study, we performed an integrated omics analyses containing WES on 314 samples, scRNA-seq on 25 samples, bulk RNA-seq on 434 samples, single-nucleus ATAC-sequencing (snATAC-seq) on 4 samples, methylation profiling by Reduced Representation Bisulfite Sequencing (RRBS) on 26 samples and lipidomics on 34 samples to systematically compare the genetic, transcriptional and microenvironmental differences between AFP$^+$ HCC and AFP$^-$ HCC. While no significant genetic differences were observed between the two subtypes, AFP$^-$ HCC exhibited pronounced activation of arachidonic acid metabolism mediated by the androgen receptor (AR), which induced substantial secretion of the downstream metabolite 11,12-epoxyeicosatrienoic acid (11,12-EET) that directly activated epidermal growth factor receptor (EGFR) on endothelial cells (ECs), thereby leading to aberrant angiogenesis. Thus, we have revealed an angiogenesis regulatory pathway controlled by AR-11,12-EET-EGFR axis in AFP$^-$ HCC, which cannot be effectively inhibited by lenvatinib. This finding provided the scientific rationale for combination treatment of lenvatinib and inhibition of AR-mediated angiogenesis for AFP$^-$ HCC.

Results

Profiling of cell diversity in the AFP$^-$ HCC and AFP$^+$ HCC

To comprehensively elucidate the distinct features between AFP$^-$ HCC and AFP$^+$ HCC, we conducted integrated omics analyses including whole-exome sequencing on 314 samples (157 tumor and 157 non-tumor adjacent tissues) from 157 patients, scRNA-seq on 25 samples (17 tumor and 8 non-tumor adjacent tissues) from 17 patients, bulk RNA-seq on 434 samples (434 tumor tissues) from 434 patients, snATAC-seq on 4 samples (4 tumor tissues) from 4 patients, methylation sequencing on 26 samples (26 tumor tissues) from 26 patients and lipidomics on 34 samples (14 tumor tissues and 20 blood plasma specimens) from 34 patients (Fig. 1a and Supplementary Fig. 1a). Clinical information of these patients was provided in Supplementary Data 1, with no significant differences in HBsAg, antiviral treatment, liver cirrhosis status, tumor number; modestly significant bias in gender, age and tumor size ($p < 0.05$); and significantly lower microvascular invasion (MVI), Barcelona Clinic Liver Cancer (BCLC) stages and Edmondson-Steiner (E-S) grades in AFP$^-$ HCC versus AFP$^+$ HCC ($p < 0.001$).

To decipher the genomic profiles of AFP$^-$ HCC, we performed WES on 157 tumors, including 44 AFP$^-$ HCC and 113 AFP$^+$ HCC, and their paired non-tumor adjacent tissues (NATs). Among them, 18,441 non-synonymous somatic mutations (range 0–636, average 117.46 per sample) and 2776 indels (range 0–420, average 17.68 per sample) across all samples were characterized. Consistent with previous findings[16–18], nine recurrently mutated genes, including *TP53*, *CTNNB1*, *AXIN1*, *ARID1A*, and *TSC2* were identified (Fig. 1b), which showed no significance between AFP$^-$ HCC and AFP$^+$ HCC (Supplementary Data 2). By identifying copy number variation (CNV) events and calculating GISTIC scores, we observed mild differences in amplification and deletion events between AFP$^-$ HCC and AFP$^+$ HCC, with significant events occupying 4% and 3%, respectively (Supplementary Fig. 1b, c). The frequently amplificated and deleted events were listed in Supplementary Data 3. In addition, no significant differences of immune editing score, clonal expansion of recurrently mutated genes and COSMIC mutation signatures were observed between the two subtypes (Supplementary Fig. 1d–g). Therefore, these results indicated that AFP$^-$ HCC and AFP$^+$ HCC patients displayed similar genomic alterations.

Next, we aimed to decipher the transcriptomic differences between the two subtypes by performing scRNA-seq on 6 AFP$^-$ HCC and 11 AFP$^+$ HCC tumor samples, with 8 paired NATs. The detailed clinical information of these patients was provided in Supplementary Data 4. The baseline of patients with scRNA-seq data was matched between AFP status groups (AFP$^-$ HCC vs. AFP$^+$ HCC). Notably, we also analyzed the paired WES data from samples with matched scRNA-seq profiles (excluding one case due to tissue unavailability). No significant differences were observed between the two HCC subtypes in terms of gene mutations, CNVs, immune editing scores, clonal expansion of recurrently mutated genes, or COSMIC mutation signatures (Supplementary Fig. 2a–e and Supplementary Data 5). In scRNA-seq data, total 210,545 single cells were collected and were classified into 47 cell types based on gene expression panorama (Fig. 1c, Supplementary Fig. 3a–d, and Supplementary Data 6). Subsequently, CNVs were inferred to validate the definition of tumor cells through inferCNV (Supplementary Fig. 3e). We then further determined that the transcriptome level of AFP in tumors was positively correlated with its serum levels in both FAH-SYSU and TCGA-LIHC cohorts (Fig. 1d and Supplementary Fig. 3f), and exhibited high expression in AFP$^+$ HCC tumor samples, with no detectable expression in tissues obtained from healthy liver, NATs of AFP$^+$ HCC, AFP$^-$ HCC tumor and NATs of AFP$^-$ HCC (Supplementary Fig. 3g). Similar results were observed in staining of FFPE specimen (Fig. 1e, f), suggesting that transcriptomic expression of AFP could represent the serum AFP level and define the two HCC subtypes.

AFP$^-$ HCC tumors presented hyperactive arachidonic acid metabolism

Next, via differential gene expression analysis based on scRNA-seq data, significantly altered genes (550 upregulated and 876 downregulated genes) in tumor cells from AFP$^-$ HCC were identified compared to AFP$^+$ HCC. The metabolism-related genes, such as *CYP2A6*, *FGGY*, and *CYP2C8*, were significantly upregulated in AFP$^-$ HCC, while proliferation-related genes such as *IGF2*, *EPCAM*, and *ARID3A*, were significantly upregulated in AFP$^+$ HCC (Fig. 2a). Consistently, Gene Set Enrichment Analysis (GSEA) suggested that the AFP$^-$ HCC tumors enriched metabolism and cell adhesion-related pathways, such as xenobiotic metabolic process, constitutive androstane receptor pathway, arachidonic acid metabolism and extracellular matrix (ECM) receptor interaction, a critical molecular feature of early-stage HCC[19], whereas the AFP$^+$ HCC tumors upregulated proliferation and carcinogenesis-associated pathways, such as Myc targets, regulation of cell division and non-canonical WNT signaling pathways (Fig. 2b). These results were also supported by previous reports[8]. To gain additional insights into the molecular differences of the two HCC

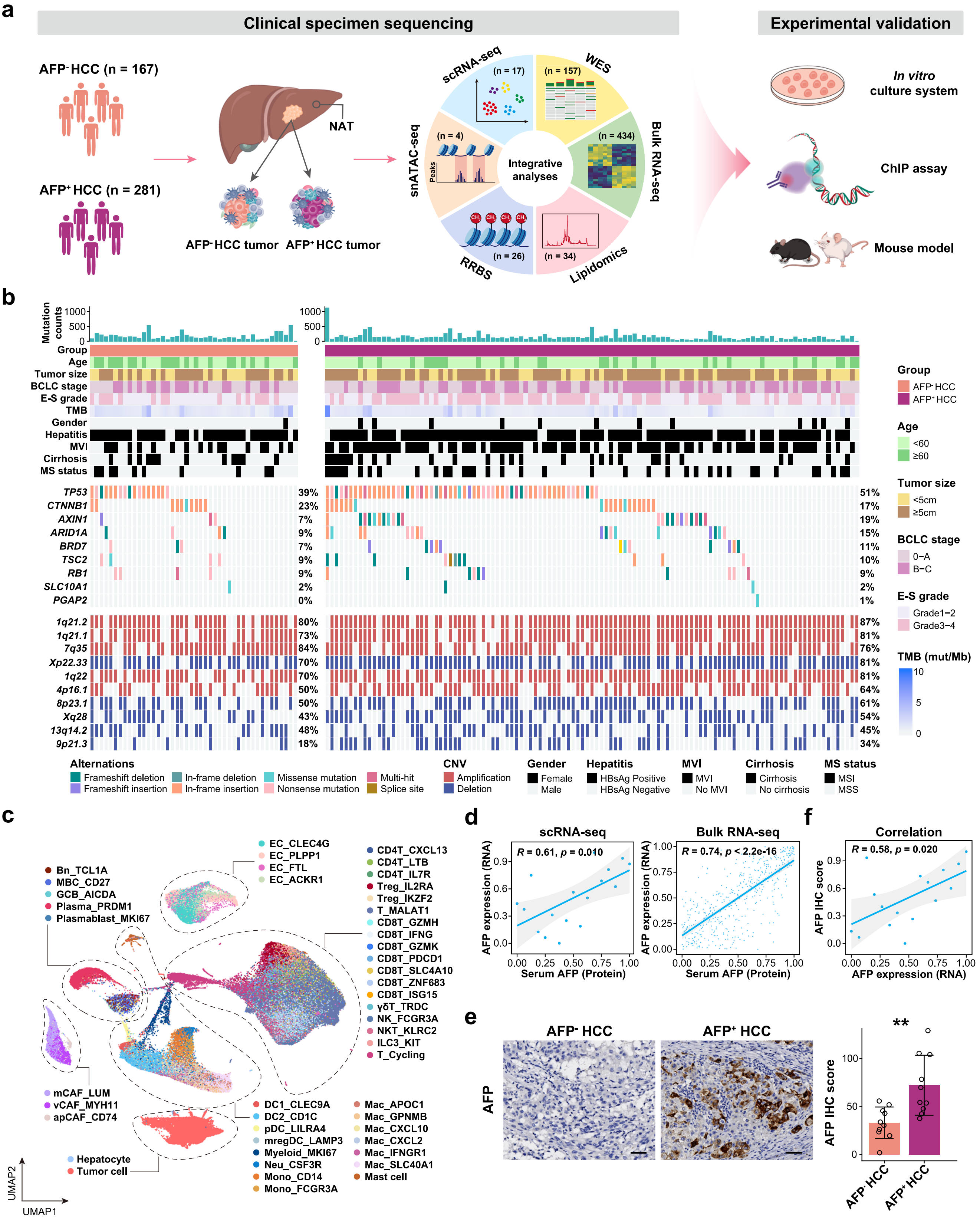

subtypes, we defined the 434 HCC patients by Hoshida's classification (Hoshida's S1, S2, and S3) based on bulk RNA-seq data using the Nearest Template Prediction (NTP) algorithm[20,21]. S1 reflected abnormal activation of the WNT and TGF-β signaling pathways; S2 was characterized by proliferation features and activation of MYC and AKT signaling, and exhibited the highest AFP expression among the three subtypes; S3 showed well differentiation of tumor cells, with the lowest AFP expression among the three Hoshida's subtypes. The results showed that AFP⁻ HCC presented similar features to the S3 subtype, whereas AFP⁺ HCC exhibited Hoshida's S1/2 subtypes characteristics (Supplementary Fig. 4a). Moreover, the differentially expressed genes (DEGs) and GSEA results from the bulk RNA-seq data also verified the

Fig. 1 | Profiling of genetic alteration and cell diversity in HCC. a Schematic overview of the research. The numbers of patients and multiple experimental validation methods are provided. The lipidomics datasets ($n = 34$) comprise two subsets: tumor tissue lipidomics ($n = 14$) and blood plasma lipidomics ($n = 20$). **b** Genetic profiles and associated clinical features of all 157 HCC patients with WES data. The top panel shows mutation numbers followed by clinicopathological features. The middle panel exhibits significantly mutated genes calculated through MutSigCV. The bottom panel shows the CNV profiles of top chromosomal lesions with the most significant q values. Different alteration types and clinical features are signified with different color codes. Significance of these variables between AFP$^-$ HCC and AFP$^+$ HCC was calculated by chi-square test or Fisher's exact test, which was provided in Supplementary Data 1. **c** The UMAP visualization of 47 cell types from scRNA-seq data. **d** Scatter plot showing positive correlation between serum AFP level and transcriptomic AFP expression in scRNA-seq (left panel) and bulk RNA-seq (right panel) data of FAH-SYSU cohort. Transcriptomic AFP expression in scRNA-seq data was calculated as the average expression across tumor cells per sample. R indicates the correlation coefficient calculated by Spearman correlation test. The number of dots indicates the number of patients. **e** Representative images of IHC staining in FFPE tissues (left panel) and protein expression of AFP in AFP$^-$ HCC and AFP$^+$ HCC (right panel). The number of dots indicates the number of patients. Scale bars, 50 μm. Data were shown as mean ± SD. $^{**}p < 0.01$ by two-sided t-test. **f** Scatter plot showing positive correlation between proteinic AFP expression and available transcriptomic AFP expression. R indicates the correlation coefficient calculated by Spearman correlation test. The number of dots indicates the number of patients. Source data are provided as a Source Data file.

---

hyperactive metabolic features in AFP$^-$ HCC and the proliferative properties in AFP$^+$ HCC (Supplementary Fig. 4b, c).

To further delineate the metabolic features in AFP$^-$ HCC, we employed the scMetabolism algorithm[22] to tumor cells from scRNA-seq data. This analysis revealed a significant upregulation of the arachidonic acid metabolism pathway in AFP$^-$ HCC (Fig. 2c and Supplementary Data 7), which exhibited a strong negative correlation with AFP expression (Fig. 2d). These findings were further confirmed by the GSEA results from scRNA-seq and bulk RNA-seq data, respectively (Fig. 2b and Supplementary Fig. 4c). Compared to all other cell types, tumor cells displayed the highest scores for arachidonic acid metabolism and the strongest difference between AFP$^-$ HCC and AFP$^+$ HCC (Supplementary Fig. 4d). Based on the well-established main branches of arachidonic acid metabolism, comprising the cyclooxygenase (COX), lipoxygenase (LOX), and cytochrome P450 (CYP) pathways[23], we conducted differential expression profiling and correlation analysis. These analyses demonstrated that CYP pathway, which generates bioactive epoxyeicosatrienoic acids (EETs) and hydroxyeicosatetraenoic acid (HETEs) to regulate cell proliferation, survival, invasion, metastasis, and angiogenesis[23], was the significantly elevated signature in AFP$^-$ HCC (Fig. 2e). Notably, the CYP pathway was the only branch exhibiting a strong negative correlation with AFP expression (Fig. 2f and Supplementary Fig. 4e, f). This observation indicated that tumor cells in AFP$^-$ HCC were more likely to reshape their metabolic patterns through the CYP pathway.

Elevation of 11,12-EET in AFP$^-$ HCC tumor cells versus AFP$^+$ HCC

In agreement with the elevated activity of CYP pathway in AFP$^-$ HCC, the CYP family genes, including *CYP2C8* and *CYP1B1*, were upregulated in AFP$^-$ HCC patients (Fig. 2g), and were confirmed by RT-qPCR assays in tumor samples (Fig. 2h). We then further sought to determine the key metabolite participating in the arachidonic acid metabolism in AFP$^-$ HCC. Through targeted lipidomics, we identified five significantly upregulated lipid-related metabolites in AFP$^-$ HCC compared to that in AFP$^+$ HCC (Fig. 2i). We decided to study 11,12-EET because: (1) the top two metabolites (ARA and DTA) served as the common substrates for COXs, LOXs, and CYPs as documented in prior studies[23–26], whereas only the CYP pathway showed significant activation in AFP$^-$ HCC; (2) 11,12-EET was the specific and direct metabolic product of the CYP pathway; (3) the upregulated CYP2C8 and CYP1B1 in AFP$^-$ HCC were the key metabolic enzymes responsible for 11,12-EET generation[23,27]; (4) elevation of 11,12-EET inversely correlated with serum AFP levels (Supplementary Fig. 4g); (5) moreover, 11,12-EET was reported to exhibit diverse biological functions[23] that might play an important role in tumor biology.

To validate the expression relation between AFP and CYPs/11,12-EET, AFP expression level in five HCC cell lines was further measured, where PLC5, Hep3B and Huh7 were defined as AFP^{high} HCC cell lines; MHCC97H and HCCLM3 belonged to AFP^{low} HCC cell lines (Fig. 2j). In line with DEGs and lipidomics analysis, AFP^{low} cell lines displayed elevated CYP2C8 and CYP1B1 expression (Supplementary Fig. 4h, i) and higher 11,12-EET levels (Fig. 2k) in comparison to the AFP^{high} cell lines, solidifying 11,12-EET as the pivotal metabolite in AFP$^-$ HCC.

Upregulated AR transcriptional activity in AFP$^-$ HCC tumor cells

Transcription factors (TF) are key molecules that control gene expression, and their activities determine the cell functions and response to intricacies of environmental disturbances[28]. Thus, to elucidate the potential regulatory mechanisms for the upregulation of arachidonic acid metabolism in AFP$^-$ HCC, we assessed the TF activity across tumor cells in scRNA-seq data using the single-cell regulatory network inference and clustering algorithm (SCENIC)[29]. The SCENIC results showed that the TF activities of MSC, KLF9, EBF1, IRF6, and AR were significantly upregulated in AFP$^-$ HCC tumor cells (Fig. 3a and Supplementary Data 8). Notably, AR transcriptional activity showed the most substantial negative correlation with AFP expression and positive association with CYP-related gene expression (Fig. 3b and Supplementary Data 9). In agreement with this finding, AR was further identified as the second most significant TF in AFP$^-$ HCC based on the bulk RNA-seq data (Supplementary Fig. 5a, b).

To further examine the TF activity of AR in AFP$^-$ HCC, we analyzed and intersected the predicted target genes of AR from scRNA-seq and bulk RNA-seq data, as shown in Supplementary Data 10 and 11, respectively. We observed that these potential AR-target genes exhibited lower methylation levels in AFP$^-$ HCC, as revealed by RRBS and TCGA-LIHC 450 K methylation sequencing, compared to those in AFP$^+$ HCC (Supplementary Fig. 5c, d). The reduced methylation of these target genes indicated the function of AR acting as a TF in AFP$^-$ HCC. Moreover, AR nuclear expression was observed significantly higher in AFP$^-$ HCC tumors than that in AFP$^+$ HCC tumors, and was significantly negatively correlated with AFP expression (Fig. 3c, d). Taken together, these findings suggested that AR might be a core TF of AFP$^-$ HCC tumor cells.

As a male hormone receptor and major oncogenic driver in prostate cancer[30], AR was also highly expressed in other cancer types, including breast cancer and HCC (Supplementary Fig. 6a). However, the role of AR in HCC is controversial. Some studies have reported the negative prognostic effect of AR in HCC patients[31], while others have demonstrated the anti-tumor functions of AR through inhibiting p38 and NF-κB pathways in HCC cells[32]. Therefore, we sought to determine the regulatory functions of AR in AFP$^-$ HCC. We observed a tightly positive correlation of AR with CYP pathway genes in HCC (Supplementary Fig. 6b). Interestingly, in addition to the upregulation of TF activity, the transcriptomic levels of AR were also upregulated in AFP$^-$ HCC tumors (Fig. 3e, f). Generally, HCC is a male-dominant cancer, and AR is highly expressed in male HCC patients[30,33]. Given the higher expression and activities of AR in AFP$^-$ HCC, we then further quantitatively analyzed plasma concentrations of testosterone and 5α-dihydrotestosterone (5α-DHT), the primary endogenous ligands of AR in HCC patients[34]. Notably, these androgen levels exhibited significant elevation in AFP$^-$ HCC compared to AFP$^+$ HCC (Fig. 3g), further suggesting that AR might be significantly activated in AFP$^-$ HCC patients.

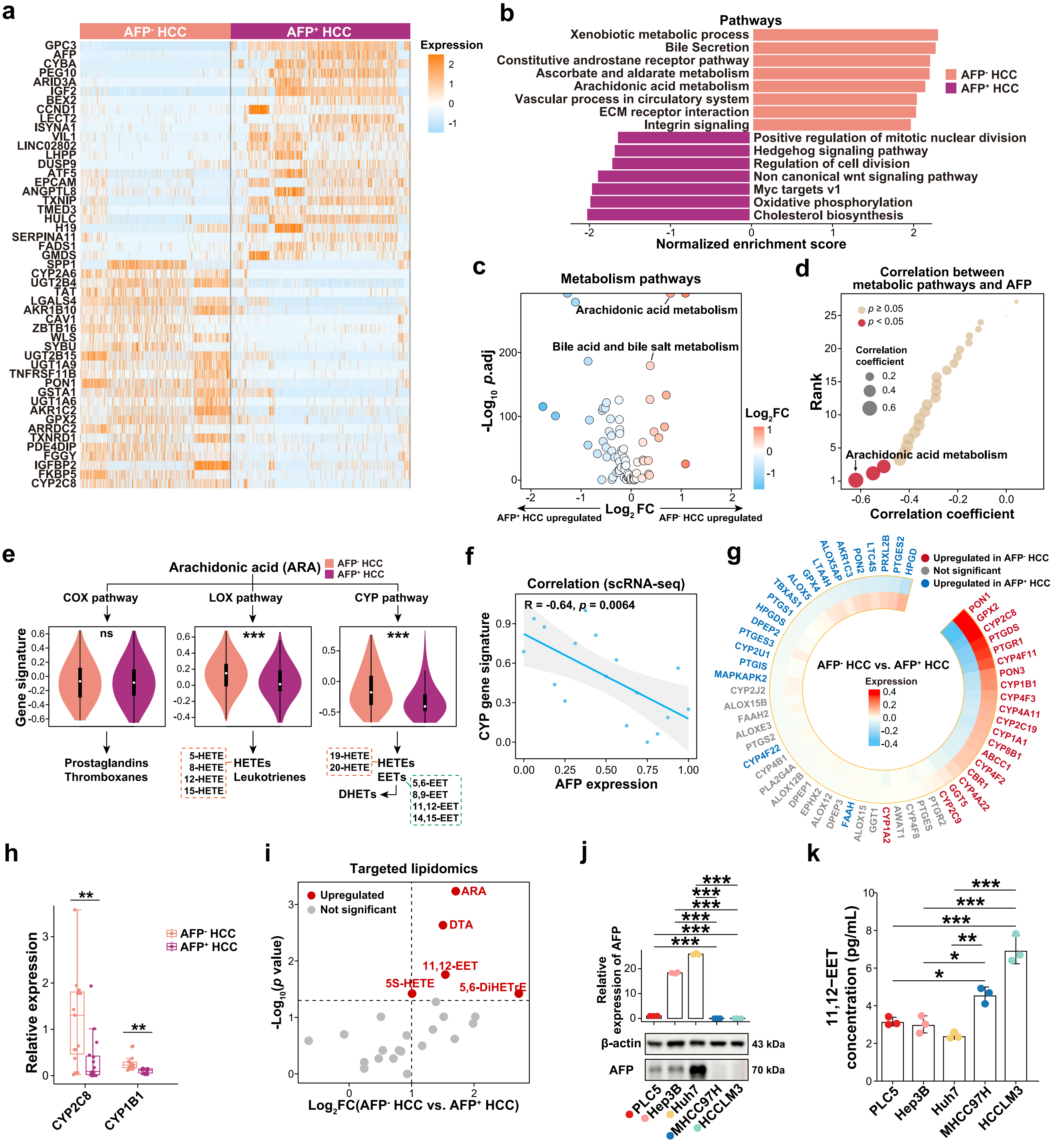

Fig. 2 | Transcriptomic differences of tumor cells between AFP$^-$ HCC and AFP$^+$ HCC. a Differentially expressed genes (DEGs) calculated from scRNA-seq data between AFP$^-$ HCC and AFP$^+$ HCC. **b** Pathways enriched in tumor cells in AFP$^-$ HCC and AFP$^+$ HCC from scRNA-seq data by GSEA. The *p*-values, calculated by permutation test, of all listed pathways were less than 0.05. **c** The volcano plot from scRNA-seq data manifested differentially metabolic activity of tumor cells in AFP$^-$ HCC when compared to AFP$^+$ HCC. The color and dot size correspond to the log$_2$FC in metabolic activity between AFP$^-$ HCC and AFP$^+$ HCC. **d** Correlation analysis between metabolic pathways and transcriptomic AFP expression in scRNA-seq data by Spearman correlation test. **e** Metabolic pathway diagram of arachidonic acid metabolism and gene signature scores of three branches in arachidonic acid metabolism. Box plot depicts the median and interquartile range, and the lower and upper hinges denote the 25–75% interquartile range (IQR), with whiskers extending up to a maximum of 1.5 times IQR. **f** Scatter plot showing negative correlation between transcriptomic AFP expression and CYP gene signature in scRNA-seq data by Spearman correlation test. **g** The heatmap of genes involved in arachidonic acid metabolism in AFP$^-$ HCC and AFP$^+$ HCC, colored by average expression value. **h** Relative expression of CYP2C8/CYP1B1 detected by RT-qPCR in tumor tissues from 15 AFP$^-$ HCC and 15 AFP$^+$ HCC patients. Data were shown as mean ± SD. **i** The volcano plot shows metabolites detected by targeted lipidomics. The abbreviations ARA and DTA stand for arachidonic acid and docosatetraenoic acid, respectively. **j** The expression levels of AFP were detected by RT-qPCR and western blot in HCC cell lines. **k** ELISA analysis revealed elevated levels of 11,12-EET in the CM derived from AFP^{low} cell lines compared to AFP^{high} cell lines. Data were shown as mean ± SD. $^*p < 0.05$, $^{**}p < 0.01$, $^{***}p < 0.001$ by Wilcoxon rank sum test in (**e**, **g**, **i**), two-sided t-test in (**h**) and one-way ANOVA with Tukey's multiple comparisons test (**j**, **k**). Source data are provided as a Source Data file.

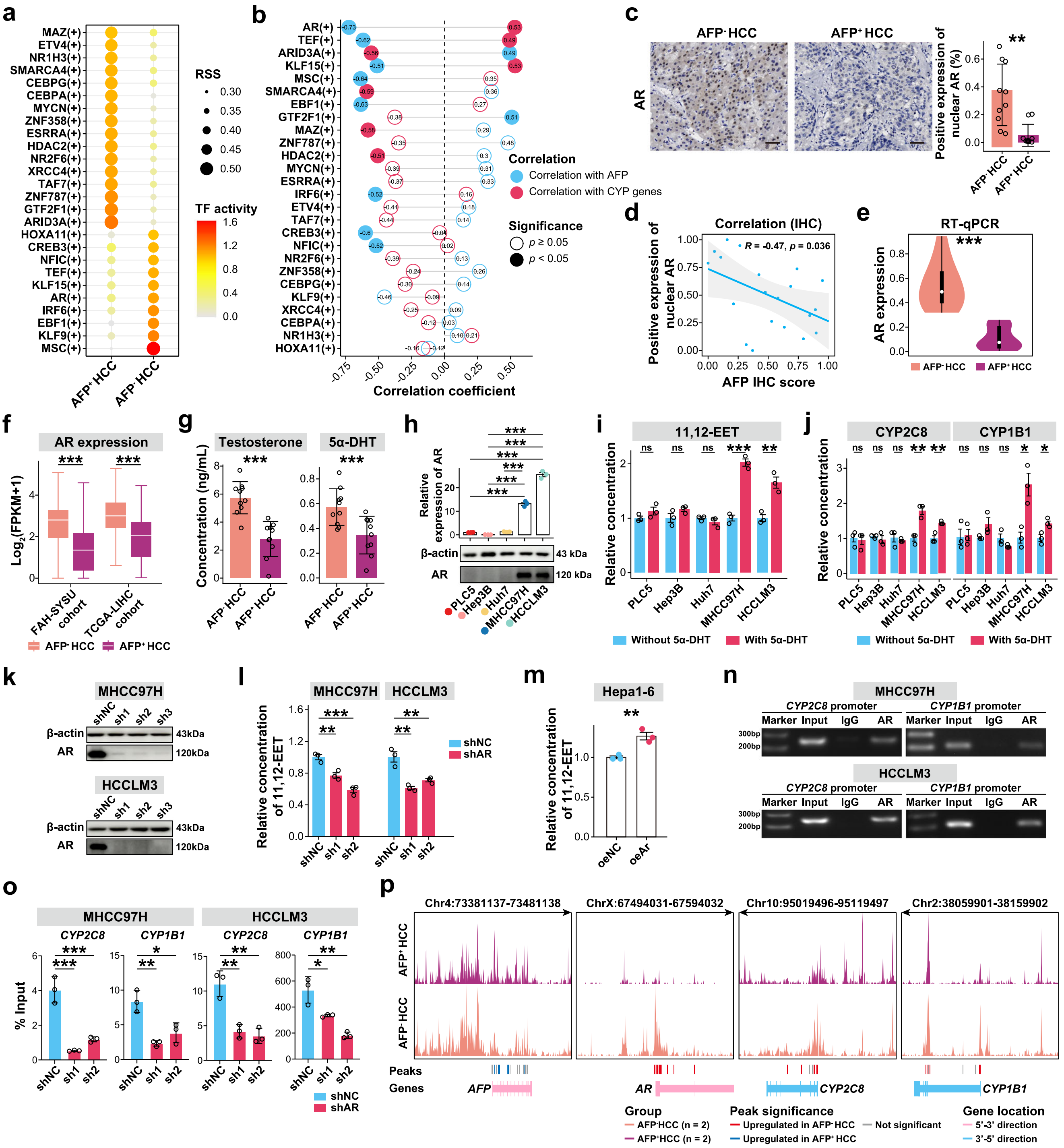

Fig. 3 | Upregulation of AR transcription activity in AFP⁻ HCC tumor cells. **a** SCENIC analysis in scRNA-seq data shows TF activities in AFP⁻ HCC and AFP⁺ HCC tumor cells. **b** Spearman correlation analysis between activity of TFs listed in (**a**), and AFP expression (colored in blue) as well as CYP genes signature (colored in red) in tumor cells. **c** Detection of AR expression using IHC in AFP⁻ HCC ($n = 10$) and AFP⁺ HCC ($n = 10$). Scale bars, 50 μm. **d** Correlation between AFP and AR expression by Spearman correlation test ($n = 20$). **e** Relative expression of AR detected by RT-qPCR (AFP⁻ HCC vs. AFP⁺ HCC = 15:15). **f** AR expression in AFP⁻ HCC compared to AFP⁺ HCC, as determined by bulk RNA-seq data from FAH-SYSU (AFP⁻ HCC vs. AFP⁺ HCC = 161:273) and TCGA-LIHC cohort (AFP⁻ HCC vs. AFP⁺ HCC = 142:127). **g** Concentrations of testosterone and 5α-DHT detected by lipidomics using blood plasma from 10 AFP⁻/AFP⁺ HCC. **h** Relative expression of AR detected by RT-qPCR and western blot in HCC cells. **i** Relative concentration of 11,12-EET detected by ELISA assays in CM from HCC cells. **j** Relative expression of CYP2C8 and CYP1B1 with or without 5α-DHT stimulation. **k** Validation of the AR knockdown (shAR) in MHCC97H and HCCLM3 using western blot. **l** 11,12-EET concentrations detected by ELISA assays in CM from MHCC97H and HCCLM3 cells (shNC) compared to their shAR counterparts. **m** Detection of 11,12-EET levels in AR-overexpressing Hepa1-6 cells (oeAr) versus control cells (oeNC). Validation of AR binding with CYP2C8 and CYP1B1 promoters by ChIP-PCR (**n**) and ChIP-qPCR (**o**) in MHCC97H and HCCLM3. **p** Normalized snATAC-seq tracks of *AFP*, *AR*, *CYP2C8* and *CYP1B1*. Three biological replicates were employed (**h**–**j**, **l**, **m**, **o**). Data were shown as mean ± SD (**c**, **g**–**j**, **l**, **m**, **o**). *$p < 0.05$, **$p < 0.01$, ***$p < 0.001$ and ns stands for no significance by Wilcoxon rank sum test (**f**, **g**), two-sided t-test in (**c**, **e**, **i**, **j**, **m**) and one-way ANOVA with Tukey's multiple comparisons test (**h**, **l**, **o**). Source data are provided as a Source Data file.

AR activates the CYP pathway to promote 11,12-EET production in AFP⁻ HCC tumor cells

To explore whether AR participated in the activation of the CYP pathway, we identified PLC5, Hep3B, Huh7 and Hepa1-6 as $AFP^{high}AR^{low}$ cell lines, while MHCC97H, HCCLM3 and RIL-175 were labeled as $AFP^{low}AR^{high}$ cell lines by RT-qPCR and western blot assays (Fig. 3h and Supplementary Fig. 6c, d). Next, $AFP^{low}AR^{high}$, but not the $AFP^{high}AR^{low}$ cell lines, boosted the production of 11,12-EET and the expression of CYP2C8 and CYP1B1 in the presence of 5α-DHT stimulation (Fig. 3i, j). In consistent with this finding, depletion of AR markedly repressed 11,12-EET production in $AFP^{low}AR^{high}$ cells (Fig. 3k, l); whereas overexpression of AR significantly promoted the production of 11,12-EET in $AFP^{high}AR^{low}$ cells (Fig. 3m and Supplementary Fig. 6e). These data together indicated the critical role of AR in regulation of the CYP pathway activity in AFP^- HCC.

Next, we aimed to elucidate whether AR could directly regulate the expression of CYP2C8 and CYP1B1. By using JASPAR database[35], we predicted AR binding sites on the CYP2C8 and CYP1B1 promoters and generated the primers. ChIP assays were then employed, and the data confirmed that AR could bind with CYP2C8 and CYP1B1 promoters (Fig. 3n). Besides, ChIP-qPCR results showed that AR depletion could significantly attenuate its TF activity on CYP2C8 and CYP1B1 (Fig. 3o). Furthermore, AFP^- HCC tumors exhibited higher chromatin accessibility signals of *AR*, *CYP2C8*, and *CYP1B1*, whereas displayed lower accessibility signals of *AFP* in comparison to AFP^+ HCC (Fig. 3p and Supplementary Data 12). Taken together, these observations indicated that AR positively regulated the CYP pathway activity in AFP^- HCC and promoted the production of 11,12-EET by enhancing the transcription of *CYP2C8* and *CYP1B1*.

Enrichment of tip-like endothelial cells in AFP⁻ HCC microenvironment

Accumulating evidence has suggested that metabolic alterations in tumor cells modulated the composition and function of surrounding cells, thereby reshaping the TME[36,37]. To study the tumor microenvironment of AFP^- HCC, we first compared the cellular composition between AFP^- HCC and AFP^+ HCC by calculating the percentage of each cell subtype relative to the total cell population in each sample using the scRNA-seq data. The analysis revealed a significant enrichment of the endothelial cell subtype EC_PLPP1 in AFP^- HCC (Fig. 4a), which was further supported by the results analyzed by the Milo algorithm[38], a statistical framework that assesses differential abundance by assigning cells to partially overlapping neighborhoods on a k-nearest neighbor graph (Supplementary Fig. 7a, b). Furthermore, the results of cellular composition were also validated by xCell deconvolution based on bulk RNA-seq data (Fig. 4b) and IHC staining of CD31, a specific biomarker of endothelial cell[39], in HCC tumor samples (Fig. 4c). Notably, the CD31 level exhibited a negative correlation with AFP expression as analyzed from the IHC data (Supplementary Fig. 7c). Altogether, these results implied that the angiogenesis ability might be a distinct signature of AFP^- HCC compared to AFP^+ HCC.

We thus further explored the distribution and function heterogeneity of endothelial cells between AFP^- HCC and AFP^+ HCC using the scRNA-seq data (Fig. 4d and Supplementary Fig. 7d). The EC_FTL with high expression of *FTH1* and *FTL*, was associated with metabolic pathways such as cell respiration, oxidative phosphorylation, and iron ion transport[40] (Fig. 4e, f). EC_CLEC4G, with high expression of canonical liver sinusoidal endothelial cell (LSEC) markers like *CLEC4G*, *CD14* and *CLEC4M*, showed preferential enrichment in NATs of AFP^+ HCC and presented active pathways related to wound healing, regulation of immune effector process, and receptor-mediated endocytosis (Fig. 4e, f and Supplementary Fig. 7d). EC_PLPP1 with expression of *IGFBP3*, *CXCR4* and *PLPP1* displayed preferential enrichment in AFP^- HCC tumor tissues, and upregulated pathways related to ameboidal-type cell migration, leukocyte migration, and endothelial development (Fig. 4e, f and Supplementary Fig. 7d), likely to be the tumor-associated endothelial cell. EC_ACKR1 with high expression of *ACKR1* and *VWF* was featured by the enriched pathways related to regulation of cell-cell adhesion, positive regulation of T cell activation, and T-helper cell differentiation (Fig. 4e, f), likely to be the venous-related endothelial cell[41].

Endothelial cells commonly exhibited two functional phenotypes in tumor angiogenesis. The tip-like endothelial cells were characterized by cell budding, migration, and formation of filopodia, while the stalk-like endothelial cell presented proliferation, adhesion, and tight connection abilities to ensure the stability of new sprouts[42,43]. Here, we observed that EC_PLPP1, enriched in AFP^- HCC, exhibited a high tip-like signature, and significantly upregulated tip-like endothelial cell-related pathways (Fig. 4g and Supplementary Fig. 7e), indicating the enhancing angiogenesis ability in AFP^- HCC.

Upregulated AR transcriptional activity promotes angiogenesis in AFP⁻ HCC

Next, we aimed to examine whether AR orchestrated the enrichment of tip-like endothelial cells in AFP^- HCC. To this end, we performed correlation analysis and found that the expression of nuclear AR was significantly positively correlated with CD31 expression (Fig. 5a). Furthermore, spatial transcriptomics analysis using a public dataset revealed that AR^+ tumor spots were in closer proximity to $PECAM1^+$ spots (namely endothelial cell spot) compared to AR^- tumor spots (Supplementary Fig. 8a, b). These results implied that AR might play a crucial role in regulating angiogenesis within the AFP^- HCC TME.

Due to the strong association between AR transcriptional activation and 11,12-EET production in AFP^- HCC, we interrogated whether AR-mediated 11,12-EET could promote sprouting angiogenesis by interacting with tip-like endothelial cells. To this end, we first predicted the binding affinity of 11,12-EET to the endothelial-specific pro-angiogenic targets by Autodock[44,45], and found that 11,12-EET exhibited the strongest binding affinity to EGFR among the candidate receptors (Supplementary Fig. 8c). Moreover, the data from surface plasmon resonance (SPR) assay confirmed that 11,12-EET could directly bind to EGFR (Fig. 5b). As a result, EGFR expression and the downstream signaling pathway were also significantly upregulated in EC_PLPP1 of AFP^- HCC (Supplementary Fig. 8d, e). We then performed in vitro assays to examine the interaction between AR-mediated 11,12-EET production and endothelial cells. The 11,12-EET treatment was shown to promote vascular migration and tube formation of human umbilical vein endothelial cells (HUVECs) (Fig. 5c). Of note, the phosphorylation level of EGFR, but not VEGFR2, was upregulated in the presence of 11,12-EET stimulation (Fig. 5d). Bulk RNA-seq data derived from HUVECs treated with 11,12-EET also confirmed the activation of EGFR-related signaling pathway, while VEGFR-related pathway remained unaffected (Supplementary Fig. 8f, g). In addition, we cultured HUVECs with the conditioned medium (CM) from $AFP^{low}AR^{high}$ cell lines (MHCC97H and HCCLM3). The results demonstrated that vascular cell migration and tube formation were robustly inhibited in the AR-knockdown group (Fig. 5e, f). Notably, we further revealed that gefitinib, an EGFR inhibitor, showed a significantly inhibitory effect on HUVEC migration and tube formation than lenvatinib in a dose-dependent manner (Fig. 5g), demonstrating that lenvatinib showed mild inhibitory effect on tumor angiogenesis in the presence of 11,12-EET stimulation in AFP^- HCC. Overall, AR-11,12-EET-EGFR axis played a critical role in promoting angiogenesis in AFP^- HCC.

AR modulates tumorigenesis and vascularization through 11,12-EET-EGFR axis in vivo

To demonstrate the eliciting effects of AR on tumorigenesis and vascularization in vivo, we established the subcutaneous HCC models using two human cell lines (MHCC97H, defined as $AFP^{low}AR^{high}$; Huh7, defined as $AFP^{high}AR^{low}$) in immunodeficient NCG mice, and two murine cell lines (RIL-175, defined as $Afp^{low}Ar^{high}$; Hepa1-6, defined as

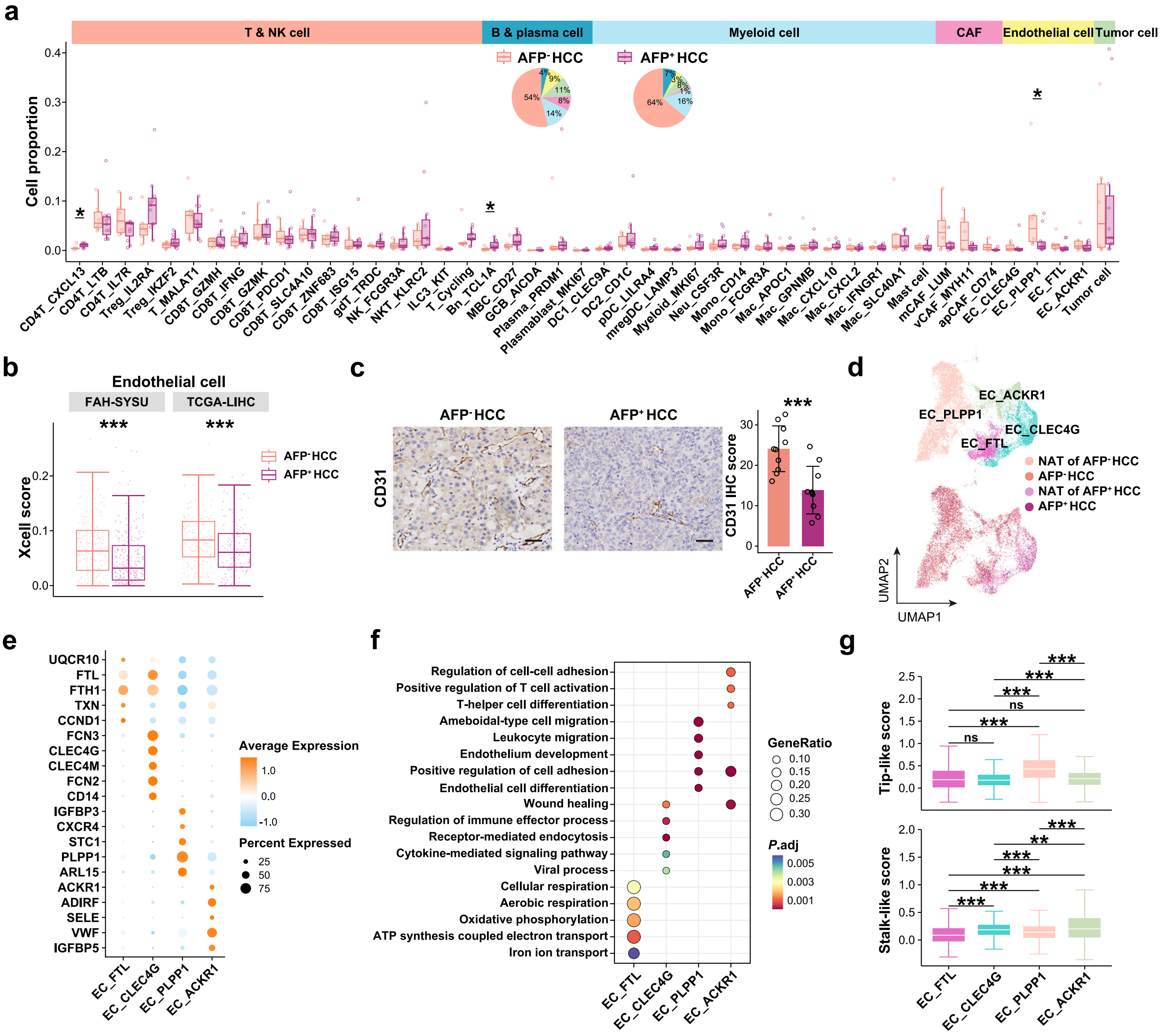

Fig. 4 | Enrichment of endothelial cells in AFP⁻ HCC. a Cell proportion analysis of each cell cluster between AFP⁻ HCC and AFP⁺ HCC patients, as shown by boxplots and pie charts. *P* values are displayed only for cell types with significant differences between the two groups (AFP⁻ HCC vs. AFP⁺ HCC = 6:11). **b** Endothelial cell proportion deconvoluted by xCell using bulk RNA-seq from FAH-SYSU cohort (AFP⁻ HCC vs. AFP⁺ HCC = 161:273) and TCGA-LIHC cohort (AFP⁻ HCC vs. AFP⁺ HCC = 142:127), which showed higher infiltration of endothelial cells in AFP⁻ HCC. **c** Representative images of IHC staining in FFPE tissues (left panel) and microvascular density quantification (right panel) in AFP⁻ HCC and AFP⁺ HCC. The number of dots indicates the number of patients (AFP⁻ HCC vs. AFP⁺ HCC = 10:10). Data were shown as mean ± SD. Scale bars, 50 µm. **d** The UMAP visualization of four subtypes of endothelial cells (upper panel) and corresponding tissue distribution (lower panel). **e** Marker gene expression for endothelial cells. **f** Pathway enrichment analysis for endothelial cells using GO-BP gene sets. **g** Functional scoring of endothelial cell phenotypes based on tip-like and stalk-like gene signatures. $^{*}p < 0.05$, $^{**}p < 0.01$, $^{***}p < 0.001$, and ns stands for not significant by Wilcoxon rank sum test in (**a**, **b**), two-sided t-test in (**c**) and Wilcoxon rank sum test with FDR correction (**g**). Source data are provided as a Source Data file.

Afp^{high}Ar^{low}) in immunocompetent C57BL/6 mice, respectively. Lentiviral transfection-mediated gene expression was performed to generate AR-knockdown counterparts for AFP^{low}AR^{high} cell lines and AR-overexpression counterparts for AFP^{high}AR^{low} cell lines (Fig. 3k and Supplementary Figs. 6e, 9a).

In NCG mice, AR knockdown significantly suppressed tumor burden, manifested as reduced invasive growth, decreased tumor volume and weight (Fig. 6a–e), accompanied with lower expression of the proliferative marker Ki67 (Supplementary Fig. 9b). In contrast, AR overexpression significantly fueled the tumor growth (Fig. 6f–i and Supplementary Fig. 9c). We further examined the expression profile of AR-11,12-EET-EGFR axis. The results showed that knockdown of AR significantly inhibited the expression levels of CYP2C8 and CYP1B1 (Supplementary Fig. 9d) as well as the production level of 11,12-EET (Fig. 6j). The expression of downstream molecule EGFR on endothelial cells (Fig. 6k) and the microvascular density (Supplementary Fig. 9e, f) were also reduced upon AR knockdown, while overexpression of AR generated significant contrast results (Fig. 6j, l and Supplementary Fig. 9g–i).

In C57BL/6 mice, similar to the results observed in NCG mice models using human HCC cell lines, knockdown of Ar significantly repressed the HCC growth and tumor angiogenesis while overexpression of Ar promoted HCC progression and vascularization within the same species (Fig. 6m–x and Supplementary Fig. 10a–h) Altogether, these data revealed the important functions of AR in regulation of tumorigenesis and vascularization in AFP⁻ HCC.

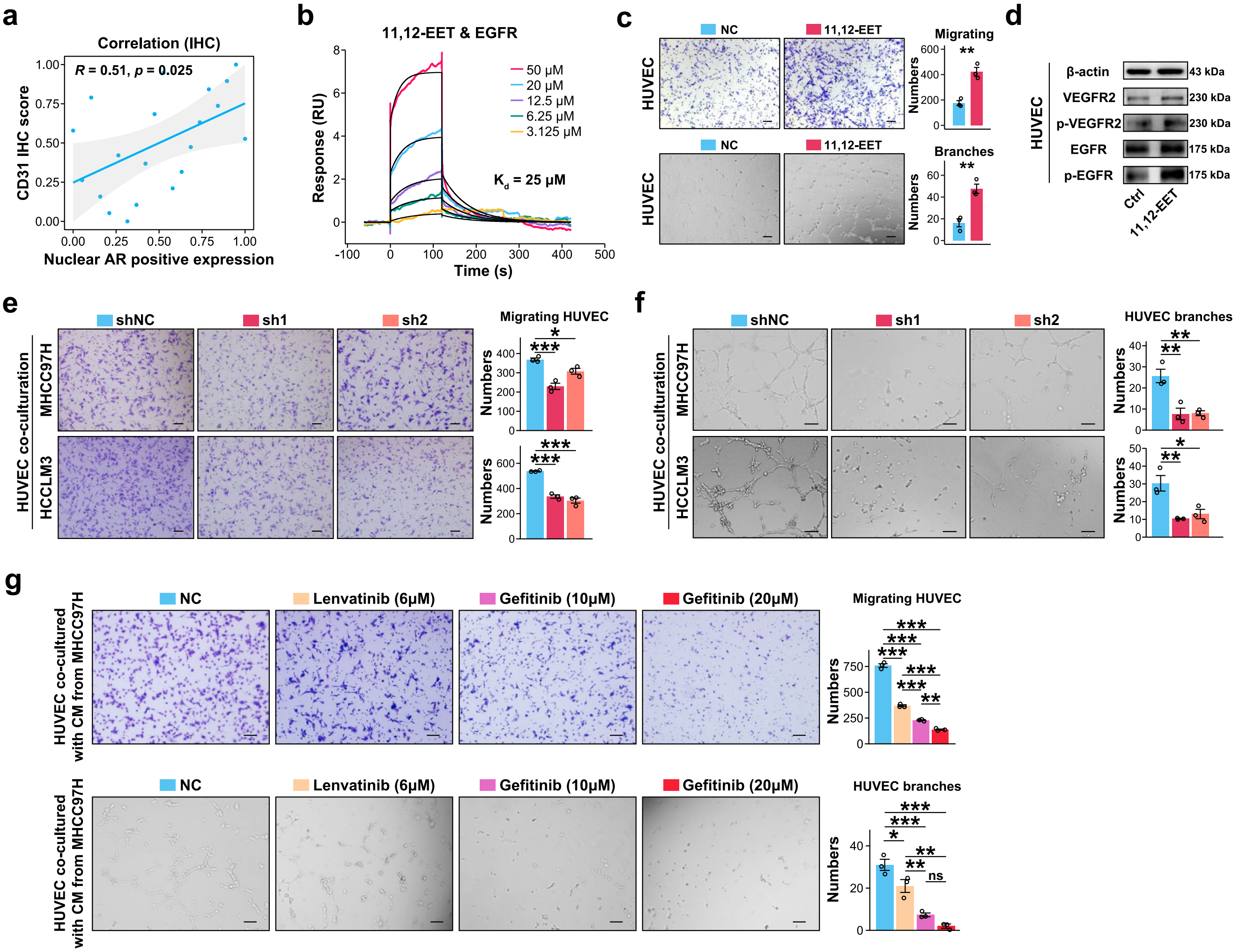

Fig. 5 | Activation of EGFR with AR-induced 11,12-EET from AFP$^-$ HCC tumor cells promoted aberrant angiogenesis. **a** Scatter plot showing positive correlation between proteinic nuclear AR expression and proteinic CD31 expression. R indicates the correlation coefficient calculated by Spearman correlation test. The number of dots indicates the number of patients. **b** Sensorgrams for detecting the binding affinity of 11,12-EET and EGFR using SPR assay. **c** Representative images (left panel) and quantitative analysis (right panel) demonstrating the pro-angiogenic effects of 11,12-EET on HUVEC migration and tube formation compared to non-11,12-EET treatment group (NC). A total of three biological replicates were employed. Data were shown as mean ± SD. **d** Protein expression of VEGFR2, phosphorylated VEGFR2 (p-VEGFR2), EGFR2 and phosphorylated EGFR2 (p-EGFR2) in HUVECs when co-cultured with 11,12-EET compared to non-11,12-EET treatment group (NC). Representative images (left panel) and corresponding statistical results (right panel) of migration (**e**) and tube formation (**f**) of HUVECs when co-cultured with the CM from shNC and shAR cell lines, including MHCC97H and HCCLM3, respectively. A total of three biological replicates were employed. Data were shown as mean ± SD. **g** Representative images (left panel) and quantitative analysis (right panel) of migration and tube formation of HUVECs when co-cultured with CM from MHCC97H. The MHCC97H cells were pre-treated with 10 nM 5α-DHT for 48 h, followed by separate treatments with either 6 μM lenvatinib, 10 μM gefitinib, 20 μM gefitinib or vehicle control for 24 h. A total of three biological replicates were employed. Data were shown as mean ± SD. Scale bars, 100 μm. $^*p < 0.05$, $^{**}p < 0.01$, $^{***}p < 0.001$ and ns stands for no significance by two-sided t-test in (**c**) and one-way ANOVA with Tukey's multiple comparisons test (**e**–**g**). Source data are provided as a Source Data file.

To further consolidate the regulatory link between AR and 11,12-EET-EGFR axis, we established an orthotopic HCC mouse model using MHCC97H cells, comprising four experimental groups: NC (control), shAR (AR knockdown), oeCYP2C8 (CYP2C8 overexpression), and shAR plus oeCYP2C8 (AR knockdown with CYP2C8 rescue) (Supplementary Fig. 11a, b). The data demonstrated that AR knockdown significantly suppressed tumor growth (Supplementary Fig. 11c, d) accompanied with reduced Ki67 (Supplementary Fig. 11e), CYP2C8/CYP1B1 expression (Supplementary Fig. 11f) and 11,12-EET production level (Supplementary Fig. 11g) as well as decreased endothelial EGFR expression level (Supplementary Fig. 11h) and microvascular density (Supplementary Fig. 11i, j), while CYP2C8 overexpression partially rescued the shAR-eliciting anti-tumor and anti-angiogenesis effects (Supplementary Fig. 11). The in vivo experimental data provided bona fide evidence supporting the regulatory role of AR in control of 11,12-EET-EGFR axis that promoted angiogenesis in AFP$^-$ HCC.

Combining AR inhibitor bicalutamide with lenvatinib suppresses tumor progression and angiogenesis in AFP$^-$ HCC in vivo

To investigate the therapeutic potential of targeting the AR-11,12-EET-EGFR for AFP$^-$ HCC, we established an orthotopic HCC mouse model by injecting MHCC97H cells into the liver lobes of NCG mice (Fig. 7a). The control and treatment groups were set as follows: (1) shNC groups including: (1) vehicle control (Ctrl); (2) gefitinib monotherapy (GEF); (3) bicalutamide monotherapy (BIC); (4) lenvatinib monotherapy (LEN); (5) bicalutamide plus gefitinib combination (BIC + GEF); (6) bicalutamide plus lenvatinib combination (BIC + LEN). (2) shAR groups including: (1) vehicle control (Ctrl); 2) gefitinib monotherapy (GEF); (3) bicalutamide monotherapy (BIC); (4) lenvatinib monotherapy (LEN); 5)

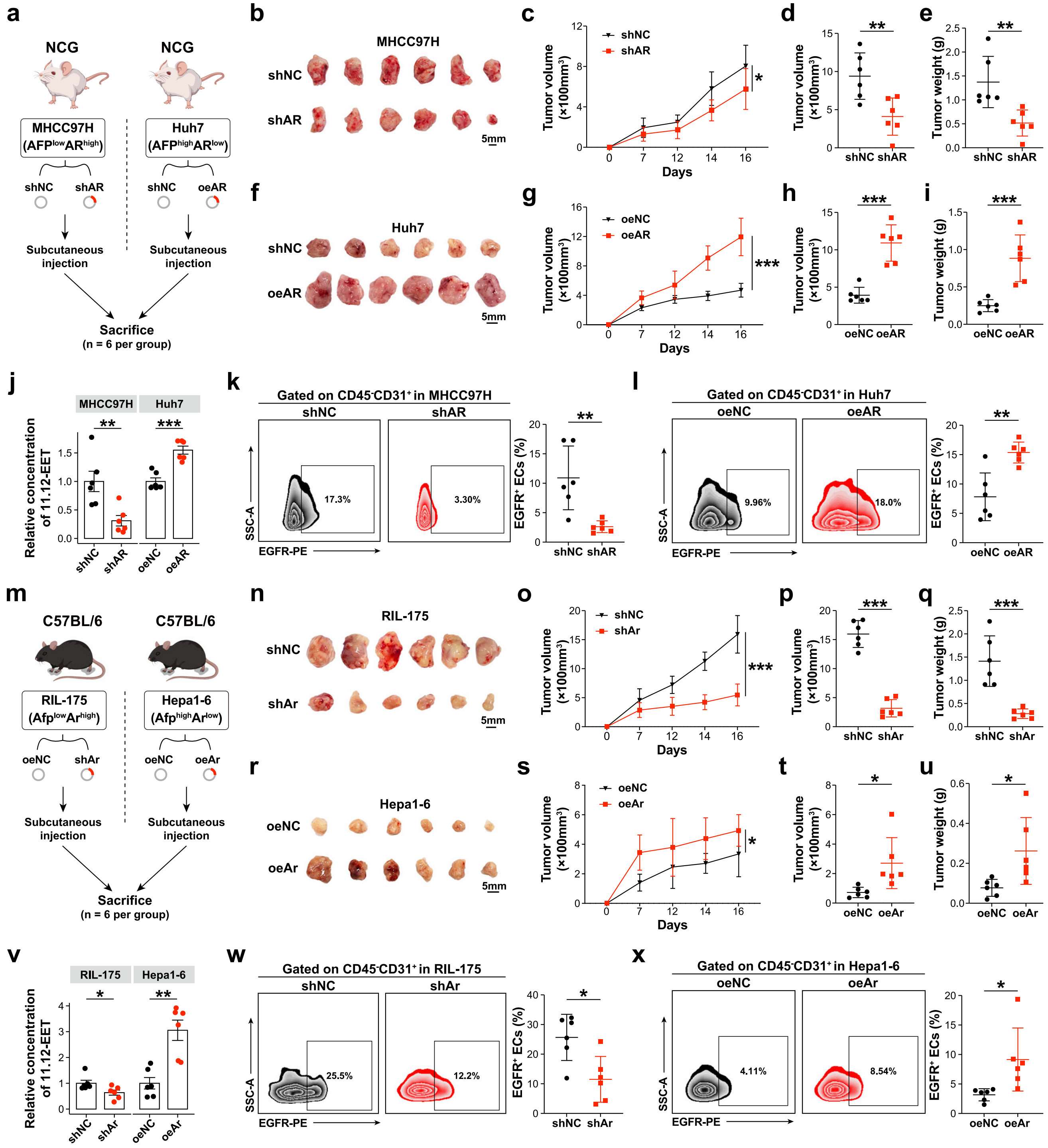

Fig. 6 | Modulation of AR in tumorigenesis and vascularization in vivo. **a** Experimental design using NCG mice ($n = 6$ per group). Representative images of tumors (**b**), tumor growth curve (**c**), tumor volume measurements (**d**) and tumor weight measurements (**e**) in MHCC97H subcutaneous HCC mouse models (shNC vs. shAR = 6:6). Representative images of tumors (**f**), tumor growth curve (**g**), tumor volume measurements (**h**) and tumor weight measurements (**i**) in Huh7 subcutaneous HCC mouse models (oeNC vs. oeAR = 6:6). **j** Relative concentrations of 11,12-EET measured by ELISA assays in MHCC97H and Huh7 subcutaneous HCC tumors, and their corresponding shAR and oeAR counterparts ($n = 6$ per group), respectively. Flow cytometry analysis of $CD45^-CD31^+EGFR^+$ endothelial cell (EC) fractions in MHCC97H (**k**) and Huh7 (**l**) subcutaneous HCC tumors ($n = 6$ per group). **m** Experimental design using C57BL/6 mice ($n = 6$ per group). Representative images of tumors (**n**), tumor growth curve (**o**), tumor volume measurements (**p**) and tumor weight measurements (**q**) in RIL-175 subcutaneous HCC mouse models (shNC vs. shAr = 6:6). Representative images of tumors (**r**), tumor growth curve (**s**), tumor volume measurements (**t**) and tumor weight measurements (**u**) from Hepa1-6 subcutaneous HCC mouse models (oeNC vs. oeAr = 6:6). **v** Relative concentration of 11,12-EET detected by ELISA kit in RIL-175 and Hepa1-6 subcutaneous HCC tumors, and their corresponding shAr and oeAr counterpart ($n = 6$ per group), respectively. Flow cytometry analysis of $EGFR^+$ ECs fractions in RIL-175 (**w**) and Hepa1-6 (**x**) subcutaneous HCC tumors ($n = 6$ per group). Data were shown as mean ± SD. $^*p < 0.05$, $^{**}p < 0.01$, $^{***}p < 0.001$ by two-way ANOVA in (**c**, **g**, **o**, **s**) and two-sided t-test in (**d**, **e**, **h**–**l**, **p**–**q**, **t**–**x**). Source data are provided as a Source Data file.

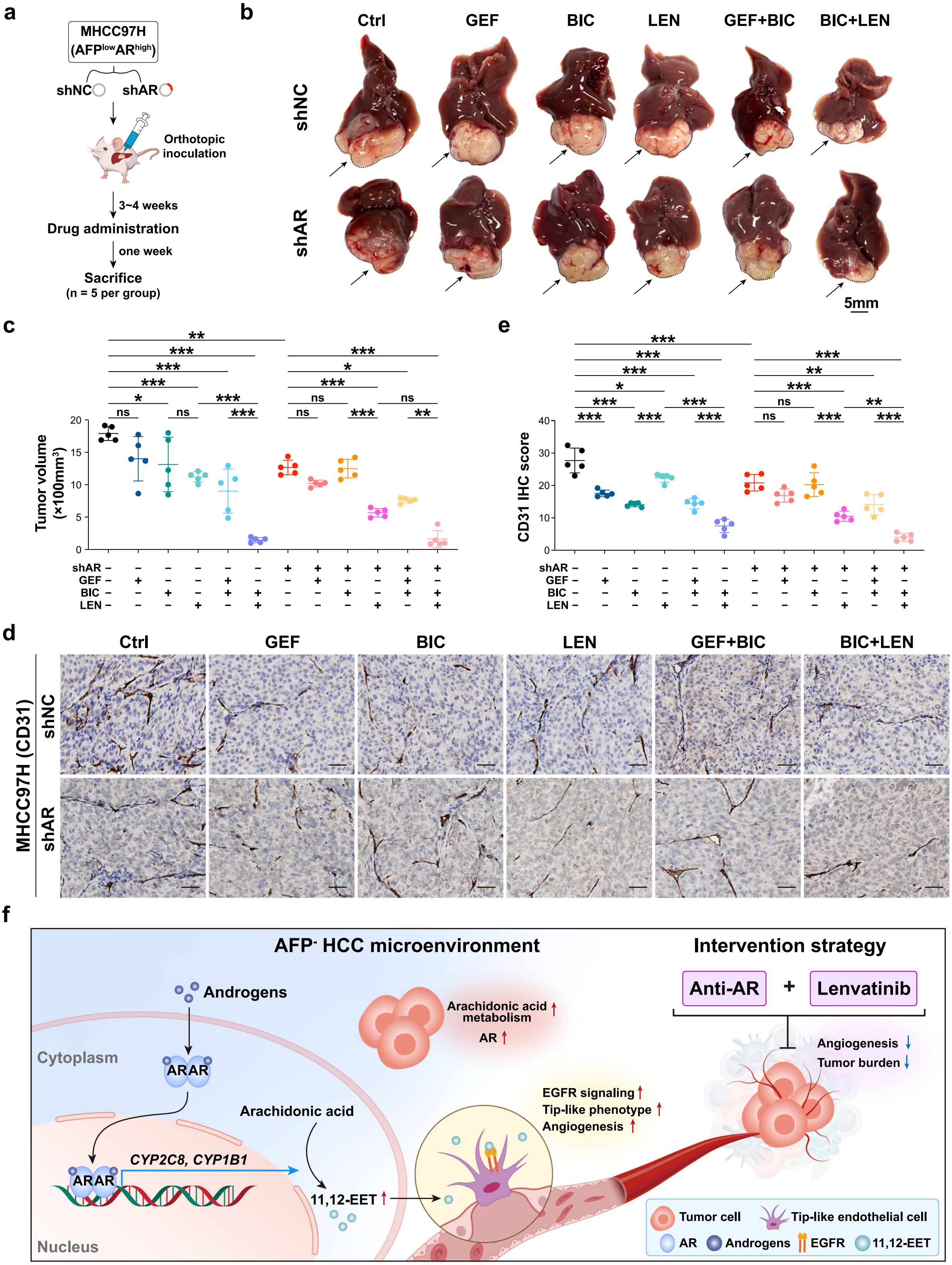

bicalutamide plus gefitinib combination (BIC + GEF); (6) bicalutamide plus lenvatinib combination (BIC + LEN).

In the shNC group, GEF monotherapy showed negligible effects on tumor burden compared to controls, whereas both LEN and BIC monotherapies elicited moderate tumor suppression (Fig. 7b, c and Supplementary Fig. 12a, b) accompanied by reduced angiogenesis (Fig. 7d, e). Notably, the combination of BIC + GEF moderately reduced the tumor growth, while the combination of BIC + LEN demonstrated the most remarkable suppression of tumor burden (Fig. 7b, c and Supplementary Fig. 12a, b).

In the shAR group, the vehicle controls (AR knockdown solo) exhibited significantly lower baseline tumor burden and microvascular

Fig. 7 | Combined inhibition of AR-mediated anti-angiogenesis with lenvatinib repressed tumor progression in AFP⁻ HCC in vivo. a Schematic of the experimental design using NCG mice ($n = 5$ per group). Representative gross images of MHCC97H orthotopic tumors (**b**) and statistical analysis of tumor volume (**c**). The "+" indicates treatment with gefitinib (GEF), bicalutamide (BIC) or lenvatinib (LEN), while the "−" indicates treatment with vehicle control ($n = 5$ per group). Data were shown as mean ± SD. **d**, **e** Representative images of IHC staining (left panel) and microvascular density quantification (right panel) in MHCC97H orthotopic tumors across different treatment groups ($n = 5$ per group). Data were shown as mean ± SD. **f** A graphical summary. In AFP⁻ HCC patients, TF activity of AR was elevated and promoted the expression levels of CYP2C8 and CYP1B1, which enhanced arachidonic acid metabolism and the production of the downstream metabolite 11,12-EET. The 11,12-EET metabolite activated EGFR on endothelial cells, thereby promoting angiogenesis. Targeting this pathway, a combination of AR antagonists with lenvatinib might represent a promising therapeutic strategy for AFP⁻ HCC. Scale bars, 50 µm. $^*p < 0.05$, $^{**}p < 0.01$, $^{***}p < 0.001$, and ns stands for no significance by one-way ANOVA with Tukey's multiple comparisons test (**c**, **e**). Source data are provided as a Source Data file.

density compared to shNC controls (Fig. 7b–e), further validating the role of AR in regulation of tumor progression and vascularization. Among the monotherapy groups, only LEN treatment significantly repressed tumor burden compared to the shAR alone. Of note, both BIC + GEF and BIC + LEN significantly damped down the tumor burden, with the BIC + LEN showing more pronounced suppressive effects in tumorigenesis and vascularization (Fig. 7b–e).

Furthermore, to solidify the synergistic effects of AR antagonist and lenvatinib, we also established a Hepa1-6 orthotopic HCC mouse model (oeNC vs. oeAR). The results showed that lenvatinib monotherapy moderately inhibited tumor growth but this inhibitory effect was significantly attenuated upon Ar overexpression (Supplementary Fig. 12c, d). Besides, combination of lenvatinib with bicalutamide significantly suppressed tumor burden, reduced Ki67 level and decreased microvascular density in the oeAr group (Supplementary Fig. 12c–f), further supporting the therapeutic potential of this combined treatment approach.

Taken together, we uncovered the hyperactive metabolic activity of arachidonic acid metabolism mediated by AR in AFP⁻ HCC, and shed insights into the mechanism of AR-induced aberrant angiogenesis, providing a promising therapeutic strategy of combining AR antagonists (e.g., bicalutamide) and lenvatinib for AFP⁻ HCC (Fig. 7f).

Discussion

In the present study, we identified arachidonic acid metabolism as a specifically activated metabolic pathway in AFP⁻ HCC, with AR being its key regulatory factor by integrated omics analysis and multiple experiments. Mechanistically, AR could promote the transcription of CYP2C8 and CYP1B1 by binding to their promoter regions, thereby enhancing the arachidonic acid metabolism that produced 11,12-EET, which activated EGFR on endothelial cells and eventually fueled tumor angiogenesis. Building on the potent roles of AR in metabolic reprogramming[46], including its regulation on lipid pathways of prostate cancer[47], and cholesterol metabolism[48] as well as glycolysis[49] in HCC, here, we unveil the impact of AR-mediated arachidonic acid metabolism on the reprogramming of AFP⁻ HCC TME, providing AR as the target for AFP⁻ HCC treatment.

To our knowledge, the role of AR in HCC remains highly controversial. AR is originally regarded as an oncogenic driver of HCC, maintaining the stemness of HCC cells and promoting cell cycle process[30,50,51]. However, parts of clinical trials have not shown significant beneficial effects of anti-androgenic therapy in HCC patients[52], and some studies showed that hepatic AR suppresses HCC metastasis[32]. These findings implied that hepatic AR might have dual but opposing roles, resulting in a dilemma in personalized treatment of HCC, and further fueling our interest in potential AR-driven TME reprogramming of AFP⁻ HCC tumors.

Furthermore, our findings demonstrated that the AR-CYP2C8/CYP1B1 axis promoted the generation of the downstream metabolite 11,12-EET, which could activate the EGFR on endothelial cells, thus inducing a tip-like phenotype in endothelial cells and ultimately leading to aberrant angiogenesis. Currently, anti-angiogenic therapy targeting VEGFRs such as lenvatinib is strongly recommended as the first-line systemic treatment for the advanced HCC and is widely applied in the clinic[53]. However, several recent global clinical trials have indicated that AFP⁻ HCC patients showed moderate treatment response to the first-line drug lenvatinib or its analogues[13–15]. Coincidentally, another study reported that HCC could be categorized into three subtypes (C1, C2, and C3) based on metabolism-related characteristic genes[54]. Among them, the C1 subtype exhibited higher metabolic activity and lower AFP expression, conferring high activity of angiogenesis-related characteristics[54], which exhibited resistant to cabozantinib, a second-line anti-angiogenic drug targeting VEGFR2[54]. In this study, we employed various animal models and demonstrated that AR^{high} HCC mice possessed higher tumor burden and vascular density than those in AR^{low} HCC mice, while combination therapy with bicalutamide and lenvatinib significantly inhibited tumor burden and vascular density in AFP⁻ HCC. Interestingly, both in vitro and in vivo findings suggested that AFP⁻ HCC might promote angiogenesis through AR-induced metabolic reprogramming and subsequent generation of 11,12-EET that binding to EGFR on endothelial cells, which might lead to the insensitivity of AFP⁻ HCC to canonical anti-angiogenic drugs.

In conclusion, our findings reveal the critical role of AR in regulation of arachidonic acid metabolism in AFP⁻ HCC and provide insights into the mechanism of AR-CYPs-11,12-EET-EGFR axis-induced tumor angiogenesis. These findings not only disclose the link between tumor metabolism and abnormal vascular growth but also highlight the promising strategy of combining AR antagonists to enhance the efficacy of lenvatinib therapy in AFP⁻ HCC.

Methods

Study approval

The study was approved by the Institutional Research Ethics Committee of First Affiliated Hospital of Sun Yat-sen University (FAH-SYSU) under Ethical Approval ID [2023]380. Informed consent, including to publish clinical information potentially identifying individuals, was obtained from all patients.

All animal experiments were performed in accordance with protocols approved by the Institutional Animal Care and Use Committee, Sun Yat-sen University (IACUC, SYSU). Approval numbers are SYSU-IACUC-2024-000262 and SYSU-IACUC-2024-000264.

Patients and samples

A total of 448 treatment-naïve patients who underwent curative liver resection at FAH-SYSU were included, with tumor samples and NAT samples. This study has received approval from the Ethics Committee of FAH-SYSU and adhered to relevant ethical standards. Clinical information of patients was summarized in Supplementary Data 1 and Supplementary Data 4. Two experienced pathologists confirmed the diagnoses through histological examinations. The sequencing types utilized in this study and their corresponding sample information were provided in Supplementary Fig. 1A.

Exome and transcriptome capture, library preparation and sequencing

For exome capture and library preparation, total DNA was extracted from snap-frozen tissues using the QIAGEN DNeasy Blood & Tissue Kit (Qiagen, Hilden, Germany). Qualified DNAs from tissue samples were fragmented into 200-300 bp fragments using Covaris technology with adapters ligated to both ends. Next, the extracted DNA was amplified by ligation-mediated PCR (LM-PCR), then purified and hybridized to NimbleGen or Agilent human exome array for enrichment. Non-hybridized fragments were washed away. For transcriptome capture and library preparation, total RNA was extracted using the Trizol (Invitrogen, USA). Poly(A) mRNA was isolated from total RNA using oligo-dT-coupled beads. The mRNA was fragmented into short fragments by adding a fragmentation buffer. Using these short fragments as templates, the first-strand cDNA was synthesized with random hexamer primers. The second-strand cDNA was then synthesized using buffer, dNTPs, RNase H, and DNA polymerase I. The short fragments were purified using the QIAQuick PCR extraction Kit (Qiagen, Hilden, Germany), dissolved in EB buffer for end reparation and adding poly(A). Next, the short fragments were ligated with sequencing adapters. Finally, exome and transcriptome libraries were constructed and loaded onto the Illumina NovaSeq 6000 sequencing platform, generating paired-end reads of 150 base pairs.

Mutation calling and annotation

FASTQ files were filtered for adapter sequences and low-quality reads using TrimGalore (v.0.6.1, https://github.com/FelixKrueger/TrimGalore). FastQC was then used to evaluate the quality of each sequencing read. Qualified reads were mapped to the human reference genome GRCh38 in paired-end mode using BWA-mem2[55] (v.2.2.1). Duplicate reads were marked using Sambamba[56] (v.0.8.2). Following GATK best practices, Mutect2[57] was then employed to detect confident somatic mutations. ANNOVAR[58] was used to annotate the final somatic mutations. Finally, MutSigCV[59] (v.1.3.5) was employed to identify significantly mutated genes with all SNVs and INDELs used as input. Genes with q-values < 0.05 were defined as significantly mutated. Tumor mutation burden (TMB), defined as the number of somatic mutations per megabase (Mb) in the coding region, was determined and quantified using our WES data. To avoid overestimating TMB, mutations with population frequencies higher than 0.05 in the Genome Aggregation Database and driver mutations curated in COSMIC database were excluded.

Detection of CNVs

CNVkit[60] (v.0.9.10) was employed to call CNVs, with tumor copy number estimates derived from BAM files using batch processing and segmentation methods. GISTIC[61] (v.2.0.23) was applied to process the results files from the previous step, identifying focal amplifications and deletions in cytoband level with amplification threshold set to 0.3, deletion threshold set to −0.3. The G-score was calculated based on the amplitude of the CNVs and its frequency of occurrence in the sample, reflecting the frequency of CNVs in the segments. To compare CNV differences between AFP$^-$ HCC and AFP$^+$ HCC patients, we first identified frequently amplified and deleted events across all patients (q value < 0.1). Next, we conducted a comparative analysis of frequently amplified and deleted events across cytobands in AFP$^-$ HCC and AFP$^+$ HCC samples. For each cytoband, we calculated the amplification or deletion frequency of CNVs in both groups and used chi-square test or Fisher's exact test with FDR adjustment to evaluate the differences. Statistical significance was defined as FDR of less than 0.05.

Microsatellite instability estimation

MSIsensor[62] was used to detect frameshift mutations in microsatellite regions and distinguish them as somatic mutations. In brief, a chi-square test or Fisher's exact test was employed to compare the length distribution of microsatellite sequences repeated at each locus between matched tumor and NAT samples. If the MSIsensor score of a sample was greater than 3.5, it was considered microsatellite instability (MSI); otherwise, it was classified as microsatellite stability (MSS).

Cancer cell fraction analysis

PyClone[63] (v.0.13.1) was used to assign somatic mutations to clonal clusters and estimate their cellular prevalence. The cancer cell fraction (CCF) of each somatic mutation was estimated based on the SNV frequency and copy number profile. For each sample, the corresponding tumor purity was used to adjust the estimated CCF.

Immune editing

Polysolver[64] (v.1.0) was employed to determine the HLA typing for each patient using the corresponding NAT sample. The non-synonymous mutations that occurred in each sample were obtained from the processed VCF file. Corresponding amino acid sequences were acquired from UniProt database, with the amino acid sequences sliding around the mutation site (9–11 residues) being selected as input. These mutated sequences, along with the HLA typing information for each sample, were collectively input into NetMHCpan[65] (v.4.0). Peptide segments with predicted binding affinities less than 500 nM were considered as immunogenic and used for subsequent analysis. The same process was applied to TCGA-LIHC cohort to construct a background condition. Finally, the immune editing score was calculated according to the literature published previously[66,67].

Mutation signature identification

SigProfilerExtractor[68] (v.1.1.21) was used to de novo decompose the mutation spectrum in the processed VCF files for all samples. The decomposed signatures were compared to known signatures from the Catalogue of Somatic Mutations in Cancer (COSMIC) database (v.3) using cosine similarity (>0.8) to determine their corresponding types. Wilcoxon rank sum test was applied to assess activity differences in contributions to each signature between AFP$^-$ HCC and AFP$^+$ HCC.

RNA sequencing data analysis

By filtering low-quality reads and removing sequencing adapters using TrimGalore (v.0.6.1, https://github.com/FelixKrueger/TrimGalore), the FASTQ files of all samples were mapped to the human reference genome GRCh38 using STAR[69] (v.2.7.9) with default parameter. The gene-level read counts and expression values in fragment per kilobase per million mapped fragments (FPKM) units were obtained using the RSEM[70] (v.1.2.28) pipeline. Based on the quantified gene read count, DESeq2[71] was employed to assess the differentially expressed genes between AFP$^-$ HCC and AFP$^+$ HCC, with a significance threshold set as adjusted p-value < 0.05 and |$\log_2$-transformed fold changes ($\log_2$FC)| > 1. GSEA[72] between AFP$^-$ HCC and AFP$^+$ HCC was conducted using pathway databases (Hallmark, KEGG, and REACTOME) from the Molecular Signatures Database (MSigDB, https://www.gsea-msigdb.org/gsea/msigdb/index.jsp). In short, all detected genes were ranked based on the $\log_2$FC between AFP$^-$ HCC and AFP$^+$ HCC for GSEA using the pre-ranked mode with default parameter settings. The xCell[73] tool was employed to estimate the proportion of endothelial cells in treatment-naïve patients from FAH-SYSU cohort and TCGA-LIHC cohort data.

Classification of HCC

To delineate the transcriptional profiles of AFP$^-$ HCC and AFP$^+$ HCC, we employed the NTP algorithm[21] to predict the molecular subtypes of HCC based on the previously published Hoshida's classification[20,21]. NTP was utilized with default parameters. Differences in Hoshida's classification were performed by chi-square test, based on methods described in previous studies[74–76]. Namely, we conducted a chi-square test and calculated the ratio of observed to expected sample numbers for each subtype (Eqs. 1 and 2).

$$X^2 = \sum \frac{(f_o - f_e)^2}{f_e} \tag{1}$$

$$R_{o/e} = \frac{f_o}{f_e} \tag{2}$$

In the equation above, X^2 represents the chi-square value. f_0 indicates the observed sample counts, while f_e denotes the expected sample counts, which can be derived from chi-square test. $R_{o/e}$ signifies the ratio of observed to expected sample counts for each subtype in different groups. If $R_{o/e} > 1$, we assumed that a subtype showed enrichment preference in a specific group.

Methylation profiling by RRBS

Methylation profiling was performed using RRBS. Briefly, a total of 50 ng genomic DNA was digested with the MspI restriction enzyme for a sufficient duration (1–3 h) to generate DNA fragments, and then ligated with a methylated adapter containing complementary sticky end. The ligated products were bisulfite-converted with sodium bisulfite using the MethylCode^{TM} Bisulfite Conversion Kit (ThermoFisher, MECOV50), PCR-amplified and purified using magnetic beads according to manufacturer's instruction. Purified library was quantified using Qubit, and then diluted to a specified concentration suitable for high-throughput sequencing. DNA library was conducted for sequencing and methylation analysis.

Methylation analysis

FASTQ files were filtered for adapter sequences and low-quality reads using TrimGalore (v.0.6.1, https://github.com/FelixKrueger/TrimGalore). FastQC was then used to evaluate the quality of each sequencing reads. Subsequently, the qualified reads were aligned to GRCh38 reference assembly and the methylation state was determined using Bismark[77] (v.0.24.1). In order to investigate whether there were differences in the methylation levels of specific genes between AFP$^-$ HCC and AFP$^+$ HCC, we calculated the methylation levels within the promoter regions, defined as the 0-1500 bp upstream of the transcription start site (TSS) of the target genes.

Generation of scRNA-seq data

Fresh tumor samples were collected within 30 min after resection and preserved in MACS Tissue Storage Solution (130-100-008, Miltenyi Biotec). Subsequently, the samples were digested into a single-cell suspension following these steps: (I) Physical slicing of the tumor tissue using a blade, followed by digestion in RPMI 1640 containing 5% FBS using Tumor Dissociation Kit (130-095-929, Miltenyi Biotec) and DNaseI (DN25-100 mg, Sigma Aldrich) for 20 min at 37 °C; (II) The digested mixture was filtered through 70 μm and 30 μm MACS strainers (130-098-462; 130-098-458, Miltenyi Biotec). Cell suspension was centrifuged at 400 x *g* for 6 min, treated with 1× Red Blood Cell Lysis Buffer (00430054, Invitrogen) for 5 min at 4 °C. Cells were washed twice with PBS, and AOPI staining was performed to assess the concentration and viability of the single-cell suspension; (III) The concentration of the cell suspension was adjusted to ~700–1300 cells/μL, followed by reverse transcription and cDNA amplification according to the standard protocol (Single Cell 5′ Reagent Kits User Guide) to prepare the library construction, and sequenced on the Illumina NovaSeq 6000.

scRNA-seq raw data processing

The raw sequencing data were processed using CellRanger (v.6.1.2, 10x Genomics). The human genome GRCh38 was used to generate expression matrices. To eliminate contamination from ambient RNA present in droplets, we applied SoupX[78] (v.1.5.2) to each sample. Cells with detectable expression of at least three genes were retained, while cells with fewer than 200 detected genes were excluded. Additionally, cells with gene counts exceeding 6000 and cells with a mitochondrial gene percentage greater than 15% were removed to ensure high-quality cells.

Normalization of the data was performed based on the raw counts using the Seurat[79] (v.4.1.0) R pipeline. The "vst" method in the Seurat FindVariableFeatures function identified the top 2000 highly variable genes for principal component analysis. A shared nearest neighbor graph was constructed using the top 50 principal components, followed by cell clustering using the Louvain algorithm. The resolution parameter was set to 0.7. Harmony[80] (v.1.0.3) pipeline was applied to remove batch effects across all samples, encompassing both malignant and non-malignant cells, using default parameters. Visualization of the results was achieved using Uniform Manifold Approximation and Projection (UMAP). Typical doublets were selected based on co-expression of lineage-specific marker genes (e.g., T/B cells, NK/myeloid cells) and subsequently removed.

Single cell CNV calling

To confirm the identification of tumor cells, we employed inferCNV (v.1.14.2, https://github.com/broadinstitute/inferCNV/wiki) to calculate CNV score for each cell. The gene expression matrix of tumor cells was extracted from the Seurat object, and CNVs were computed using cancer-associated fibroblasts and endothelial cells as references. The parameters used were "denoise" = TRUE, "hidden Markov model (HMM)" = TRUE and with a "cutoff" value of 0.1 for inferCNV analysis.

Differential expression analysis and pathway enrichment analysis in scRNA-seq data

For tumor cells, FindMarkers function from Seurat package was employed to perform Wilcoxon rank sum tests on the normalized expression data obtained during data processing. The parameters were set as min.pct = 0.25, logfc.threshold = 0, resulting in the identification of differentially expressed genes (DEGs) between AFP$^-$ HCC and AFP$^+$ HCC cells. GSEA for AFP$^-$ HCC and AFP$^+$ HCC was conducted using pathways from the Hallmark, KEGG, and REACTOME databases within MSigDB. In summary, all detected genes were ranked based on $\log_2$FC between AFP$^-$ HCC and AFP$^+$ HCC, serving as input for GSEA. The local GSEA software was executed in pre-ranked mode with default parameter settings. For pathway enrichment in endothelial cells, we utilized the significant DEGs with adjusted p-value < 0.05 for Gene Ontology (GO) enrichment analysis using ClusterProfier[81] (v.4.9.0.002) package. Pathways with an adjusted p value < 0.05 were considered significantly enriched.

Analysis of metabolism activity

In order to estimate single-cell level metabolic activity, we employed scMetabolism[22], a computational pipeline for calculating metabolic activity using scRNA-seq data. Taking the UMI count expression matrix of the Seurat object as input, single-cell metabolism analysis was conducted using the "VISION" method, generating a high-quality list of metabolic gene sets based REACTOME database[82].

Calculation of gene signature score

We assessed the arachidonic acid metabolic activity of tumor cells using Gene Set Variation Analysis (GSVA)[83] package with the parameter method as "gsva", utilizing gene sets from REACTOME[82]. Based on tip and stalk signatures from published literature[43], we used GSVA to evaluate tip-like and stalk scores for endothelial cells.

Analysis of TF activity

To assess the TF regulatory activity of tumor cells in AFP$^-$ HCC and AFP$^+$ HCC in scRNA-seq data, we employed the single-cell regulatory network inference and clustering (pySCENIC, v.0.12.1) workflow[29,84] with parameters recommended by the official documentation. SCENIC defines the regulons, which comprise the TF and its potential target genes for each cell and assesses the regulon's activity. The TF activity level indicates the predicted influence of the TF within the cell, with higher activity reflecting a stronger influence. Auxiliary datasets were obtained from the website (https://resources.aertslab.org/cistarget/). We employed the commands pyscenic grn, pyscenic ctx, and pyscenic aucell to infer the gene regulatory network, predict regulons, and calculate cellular enrichment (area under the curve, AUC) for each processed cell. Finally, the calcRSS[85] function was used to visualize the specific activated TFs in AFP$^-$ HCC and AFP$^+$ HCC tumor cells. Additionally, we utilized the corto[86] R package to predict the TF activity in AFP$^-$ HCC and AFP$^+$ HCC with bulk RNA-seq data.

Correlation analysis

The correlation was performed using the Spearman correlation test, including correlation between genes, between gene and signature scores or TF activities, and between IHC protein expression scores. For scRNA-seq-based comparisons of variables such as AFP expression of tumor cells versus serum AFP levels, we first obtained the pseudo-bulk expression profile of tumor cells using the AverageExpression function in Seurat. Based on this profile, we extracted the average AFP expression levels of tumor cells for each patient. To address the differences in quantitative scales between transcriptome sequencing and serum testing, we normalized both the average AFP expression levels and serum AFP levels using min-max normalization to a range of 0–1. Finally, Spearman correlation analysis was performed on the normalized values to examine the relationship between the two variables. The same computational method was applied for the correlation analysis of bulk RNA-seq data.

The min-max normalization was performed using the formula:

$$V_{scaled} = \frac{V_i - V_{\min}}{V_{\max} - V_{\min}}$$

Where V_{scaled} and V_i represent the scaled and unscaled value of the variable in each sample, respectively. In the formula, $V_{\max}$ and $V_{\min}$ represent the maximum and minimum values of the variable in all patients.

Differential cell abundance analysis

The differences in cellular abundance between tumor samples from AFP$^-$ HCC and AFP$^+$ HCC patients were calculated using different methods. One approach focused on calculating the proportion of each cell type relative to the total number of cells in each sample, followed by a Wilcoxon rank sum test to compare cell abundances between AFP$^-$ HCC and AFP$^+$ HCC patients. Another approach utilized was the MiloR[38] (v.1.6.0) workflow, a scalable statistical framework, to compare cellular abundance differences between the two groups. Milo performs differential abundance testing by assigning cells to partially overlapping neighborhoods on a k-nearest neighbor (KNN) graph. We first constructed the KNN graph using the buildGraph function based on scRNA-seq data, and recommended tutorial parameters were used. Next, we used the makeNhoods function to assign cells to neighborhoods based on their connectivity on the KNN graph. The AFP$^-$ HCC and AFP$^+$ HCC groups were set as test variables in the testNhoods function. The $\log_2$FC in cell numbers between the two groups in each neighborhood was used for visualization. Significantly differentially abundant neighborhoods were detected in AFP$^-$ HCC-enriched neighborhoods (Spatial FDR < 0.1 and $\log_2\text{FC} > 0$) and AFP$^+$ HCC-enriched neighborhoods (Spatial FDR < 0.1 and $\log_2\text{FC} < 0$).

snATAC-seq data generation

Nuclei suspensions were prepared from tumor specimen and incubated in a Transposition Mix that includes a Transposase to complete the transposition process. Gel Bead-in-Emulsion (GEM) was then generated by combining barcoded Gel Beads, transposed nuclei, a Master Mix, and Partitioning Oil on a Chromium Chip E. In order to achieve single-nucleus resolution, nuclei were provided at a certain dilution, such that the majority (~90–99%) of generated GEMs did not contain nuclei, while the remaining majority contained a single nucleus. After eliminating unused barcodes from the sample, P7, a sample index, and Read 2 (Read 2 N) sequence were added during library construction via PCR. The final libraries contained the P5 and P7 primers used in Illumina bridge amplification, and then sequenced on Illumina NovaSeq 6000 platform according to Chromium Single Cell ATAC protocol.

snATAC-seq data analysis

CellRanger-atac count (v.2.1.0, 10x Genomics) pipelines were used to process sequenced snATAC-seq data, aligned to GRCh38 human reference. To call peaks on snATAC-seq data, Signac[87] (v.1.10.0) R package and ArchR[88] (v.1.0.2) R package were imported. Briefly, the filtered peak-count matrix was normalized by employing term frequency-inverse document frequency (TF-IDF) normalization from the Signac package. Next, peaks with the highest frequency among cells were chosen. RunSVD Signac function was employed to perform singular value decomposition (SVD) on the normalized TF-IDF matrix to obtain a lower-dimensional representation of all cells, after which SVD embeddings were used for dimensionality reduction and clustering. Then, GeneActivity function in the Signac package was used to estimate transcriptional activity for each gene by quantifying snATAC-seq read counts at promoter region of the gene body. Malignant cells in the snATAC-seq data were identified and extracted based on the gene activity of malignant cell markers (e.g., *APOA2*, *TTR*, *GPC3*, and *AKR1B10*). Besides, createArrowFiles, ArchRProject and plotBrowserTrack function in the ArchR package pipeline with recommended parameters were utilized to call peak from malignant cells. Finally, the differences of snATAC peaks called by MACS2 (v.2.2.8) between AFP$^-$ HCC and AFP$^+$ HCC tumor cells were identified using the getMarkers function with default parameters, using a threshold set at FDR < 0.05 and $|\log_2\text{FC}| > 0.5$ to determine the differential peaks between the two groups.

Lipidomics

Targeted lipidomics was utilized to detect the lipid-associated metabolites, which is a specialized branch of lipidomics that focuses on the quantitative analysis of specific lipid species within a biological sample. Unlike untargeted lipidomics, which aims to profile a broad range of lipids, targeted lipidomics concentrates on predefined lipid molecules of interest, primarily the metabolites associated with the arachidonic acid metabolism pathway in our study. This approach enables precise and accurate quantification of relevant lipid molecules, facilitating the investigation of their roles in various biological processes and disease states. Additionally, the targeted lipidomics was performed using Ultra-High Performance Liquid Chromatography coupled with Tandem Mass Spectrometry (UHPLC-MS/MS). The detailed protocols for sample preparation, metabolite quantification, and compound annotation in the lipidomics analysis were provided in the Supplementary Methods. The detailed list of the chemical standards used for targeted lipidomics analysis, along with their corresponding detection parameters was provided in Supplementary Data 13. We obtained and compared the final concentrations of metabolites associated with lipid oxidation and steroid lipidomics hormone to identify the metabolic differences between AFP$^-$ HCC and AFP$^+$ HCC patients.

Binding affinity detection

To determine whether 11,12-EET can potentially bind to druggable targets in endothelial cells, AutoDock Tool was used to prepare files for molecular docking using AutoDock Vina[44,45]. Firstly, the three-dimensional (3D) structure of 11,12-EET was downloaded from the PubChem website (https://pubchem.ncbi.nlm.nih.gov/), which was then converted into a PDB file using openbabel[89] (v.3.1.1), added with hydrogen atoms, set as a ligand and exported as a PDBQT file. Next, the protein 3D structures of the target were downloaded from the Protein Data Bank website (PDB, https://www.rcsb.org/). Water molecules were removed from the protein structure, and hydrogen atoms were added. The protein was subsequently designated as the receptor and exported as a PDBQT file. Then, the PDBQT files of the receptor and ligand were imported into the AutoDock Tool program, and the grid box size was adjusted to encompass the active pocket. Finally, docking calculation was carried out via AutoDock Vina.

Surface plasmon resonance

Surface plasmon resonance (SPR) assay was used to determine the affinity of EGFR with 11,12-EET. The activator was prepared by mixing 400 mM EDC and 100 mM NHS immediately before injection. The CM5 sensor chip (29149603, Cytiva) was then activated for 420 s with this mixture at a flow rate of 10 μL/min. EGFR (ab155639, Abcam) was diluted to 30 μg/mL in immobilization buffer and injected into the sample channel (Fc4) at a flow rate of 10 μL/min, typically achieving immobilization levels of 3400 RU. The reference channel (Fc3) did not require the ligand immobilization step. The chip was deactivated using 1 M Ethanolamine hydrochloride at a flow rate of 10 μL/min for 420 seconds. 11,12-EET (50511, Cayman Chemical Company) was diluted with the same analyte buffer to six different concentrations (50, 25, 12.5, 6.25, 3.125, and 0 μM). It was then injected into channels Fc3 and Fc4 at a flow rate of 30 μL/min for an association phase of 120 s, followed by a dissociation phase of 300 s. Both the association and dissociation processes were carried out in the analyte buffer. Six cycles of analyte injections were performed in ascending concentration order. After each cycle of interaction analysis, the analyte was allowed to dissociate naturally. The chip did not require regeneration between cycles. Finally, the affinity constant was calculated.

Immunohistochemistry staining

The formalin-fixed paraffin-embedded (FFPE) tumor specimens were cut into 4 μm-thick slides for subsequent Immunohistochemistry (IHC) staining. Slides were placed in a 65 °C oven for 4 hours. Deparaffinization and rehydration were carried out using xylene and different gradient concentrations of ethanol. Heat-induced antigen retrieval was performed with indicated solution. Endogenous peroxidase activity and non-specific staining were blocked using 3% H_2O_2 and 10% goat serum, respectively. The primary antibodies were incubated overnight at 4 °C. After incubation, the slides were washed three times with PBS, followed by incubation with the secondary antibody for 30 min. Subsequently, the slides were washed with PBS, and the antigen-antibody reaction was visualized using 3,3'-diaminobenzidine. Finally, the slides were counterstained with hematoxylin, dehydrated through a series of graded ethanol, cleared in xylene, dried, and sealed with coverslips. Images were obtained using a digital pathology slide scanner (Kfbio, China). The concentrations and sources of the primary antibodies used for IHC were as follows: AFP, 1:600 (ab133617, Abcam, for human specimen); Afp, 1:500 (ab46799, Abcam, for mice specimen); AR, 1:250 (ab133273, Abcam, for human and mice specimen); CD31, 1:500 (ab28364, Abcam, for human specimen); Cd31, 1:1500 (ab182981, Abcam, for mice specimen); Ki67, 1:500 (12202S, CST, for human and mice specimen); CYP2C8, 1:100 (PA5-101311, Invitrogen, for human and mice specimen); CYP1B1, 1:500 (PA5-95277, Invitrogen, for human and mice specimen).

Protein expression based on IHC

Expression of AFP, CYP2C8 and CYP1B1 was assessed through a positive staining score. In brief, the positive staining score is the product of the protein staining intensity and the percentage of immunoreactivity. The staining intensity of protein was graded on a scale of 0-3, where 0 indicates no staining, 1 indicates weak immunoreactivity, 2 indicates moderate immunoreactivity, and 3 indicates strong immunoreactivity. The percentage and identification of immunoreactivity for each slide were acquired from Image J with IHC Profiler. For IHC score of AR and Ki67, we manually counted the number of AR- or Ki67-positive nuclei in HCC cells and divided it by the total number of HCC cell nuclei in each filed. As for IHC score of CD31, we counted the number of positively stained vessels in each filed. The staining intensity of blood vessels was divided into three levels, 1 for light brown, 2 for medium brown, and 3 for dark brown. The final CD31 IHC score was obtained by multiplying the number of positively stained vessels by the staining intensity. For each slide, the average IHC score for each protein expression (e.g., AFP, CYP2C8, CYP1B1, AR, Ki67 and CD31) was calculated by randomly selecting three individual low-power fields and visualized in ggplot2 (v.3.4.4) R package.

Cell lines

The human HCC cell lines PLC5, Hep3B and Hepa1-6 were obtained from ATCC. Huh7, MHCC97H and HCCLM3 were obtained from Cell Bank of Typical Culture Preservation Committee of Chinese Academy of Science, Shanghai, P.R. China. RIL-175 cells were kindly provided by Prof. Alfred Sze-Lok Cheng. HUVECs were obtained from Meisen Chinese Tissue Culture Collections, Zhejiang, P.R. China. All cell lines were confirmed to be free from mycoplasma contamination and authenticated using short tandem repeat (STR) profiling. All cell lines except for HUVEC were cultured in DMEM (C11995500BT, Gibco) supplemented with 10% fetal bovine serum (FBS) (10099141, Gibco) and 1% Penicillin-Streptomycin (15140163, Gibco). HUVECs were cultured in EGM™-2 Endothelial Cell Growth Medium-2 BulletKit™ (CC-3162, Lonza). All cell lines were maintained in a humidified atmosphere at 37 °C with 5% CO_2.

Lentiviral vectors expressing short hairpin RNA (shRNA) targeting AR (shAR) or a control sequence (shNC), as well as vectors carrying AR or CYP2C8 overexpression plasmids (oeAR) or a control sequence (oeNC), were procured from VectorBuilder (https://www.vectorbuilder.cn/, China). The MHCC97H and HCCLM3 cell lines were transfected with shAR or shNC lentiviral vectors, while the Huh7 cell line was transfected with oeAR or oeNC lentiviral vectors. Similarly, the RIL-175 cell line was transfected with shAr or shNC lentiviral vectors, and the Hepa1-6 cell line was transfected with oeAr or oeNC lentiviral vectors. Additionally, the MHCC97H cell line was transfected with lentiviral vectors carrying CYP2C8 overexpression plasmids (oeCYP2C8) or a control sequence. Following transfection, clonal cells were selected using puromycin or G418 for seven days. The successful constructions of AR-knockdown, AR-overexpressing, CYP2C8-overexpressing and AR-knockdown plus CYP2C8-overexpressing HCC cell lines were validated by western blot analysis.

Reverse transcription-quantitative polymerase chain reaction

Total RNA was extracted using TRIzol reagent (Invitrogen). Reverse transcription of 1 μg RNA into cDNA was performed using the Reverse Transcription Master Kit (Takara) following the manufacturer's instructions. Reverse transcription-quantitative polymerase chain reaction (RT-qPCR) analysis was conducted using SYBR green (SYBR® Premix Ex Taq™ II, Takara) on the QuantStudio™ 7 Flex real-time PCR system (Applied Biosystems). The values were normalized to the expression level of GAPDH mRNA, and the relative expression level was calculated using the $2^{-\Delta\Delta CT}$ method. The primer sequences used for RT-qPCR assays are shown in Supplementary Data 14.

Chromatin immunoprecipitation assay

Chromatin immunoprecipitation (ChIP) assay was performed using the NovoNGS CUT&Tag 2.0 High-Sensitivity Kit (N259-YH01, NovoProtein) according to the manufacturer's protocol and instructions. Briefly, after stimulation with 10 nM 5α-DHT for 24 h, cells were trypsinized and enriched using ConA-magnetic beads. The cell suspension was incubated with anti-human AR primary antibody (ab108341, Abcam) overnight at 4 °C. The beads were washed and incubated with the secondary antibody at a concentration of 10 μg/ml for 1 h. After washed in Dig-Hisalt Buffer, the beads were incubated with proteinA-Tn5 transposome in ChiTag Buffer at room temperature for 1 h. Subsequently, the cells were mixed in labeling buffer at 37 °C for 1 h. The tagmentation reaction was stopped by adding stop buffer and incubating at 55 °C for 10 min. Tagment DNA was extracted using Extract

Beads and subjected to PCR. The primer sequences for promoter regions of *CYP2C8* and *CYP1B1* were designed based on predicted binding sequences of AR using "Scan" mode in JASPAR database (https://jaspar.elixir.no/), which was shown in Supplementary Data 14.

Western blot

The cultured cells were dispersed in RIPA lysis extraction buffer (PC101, Epizyme Biotech) with protease and phosphatase inhibitor cocktail (04906845001, Roche) added, followed by incubation for 30 min. The cell lysates were centrifuged at 12,000 × *g* for 10 min at 4 °C. The supernatant was collected and assessed for protein concentration using the BCA protein concentration determination method. Subsequently, SDS loading buffer was added to the protein samples and boiled at 95 °C for 7 minutes. A total of 20 μg protein was separated by 10% SDS-polyacrylamide gel electrophoresis and transferred onto a pre-equilibrated nitrocellulose membrane (IPVH00010, Merck). The membrane was blocked with protein-free rapid blocking buffer and then incubated with specific primary antibody overnight at 4 °C, including β-actin (4970 L, CST), AFP (ab133617, Abcam, for human samples; ab46799, Abcam, for murine samples), AR (ab133273, Abcam, for human samples; ab52615, Abcam, for mice samples), CYP2C8 (16546-1-AP, Proteintech), VEGFR2 (9698S, CST), p-VEGFR2 (2478S, CST), EGFR (ab52894, Abcam), and p-EGFR (ab40815, Abcam). Secondary antibody was then incubated for one hour at room temperature. Finally, the membranes were incubated with Super-Signal West Pico substrate, and the protein signals were detected using the Amersham Imager 800 imaging system (GE, USA).

ELISA

The concentration of 11,12-EET in both the CM and the tissue was measured using the enzyme-linked immunosorbent assay (ELISA) kit (11E39-K01, Eagle Biosciences), according to the manufacturer's instructions. CM was collected from HCC cell lines pretreated with or without 10 nM 5α-DHT (A8380-1G, Sigma-Aldrich). For tumor tissue samples, 80 mg of tumor tissues was homogenized on ice in lysis buffer. The homogenates were then centrifuged at 4 °C to obtain the supernatant fraction. After sample preparation, standard curves were generated alongside sample analysis by preparing serial dilutions of known molecular concentrations. Aliquots of standards and samples were loaded into microplate wells, incubated with the kit's detection reagents, and then washed according to the kit protocol. The optical density was read at the 450 nm using a microplate reader, and concentrations of 11,12-EET were calculated based on the corresponding standard curves. Samples were measured in triplicate to ensure data accuracy and reproducibility.

Flow cytometry

Fresh tumor samples from mice were minced into ~1 mm^3 pieces in RPMI 1640 medium supplemented with 10% FBS and enzymatically dissociated using the MACS Tumor Dissociation Kit for 30 min at 37 °C. The resulting cell suspension was filtered through a 70 μm cell strainer. Red blood cells were then removed using RBC Lysis Buffer, followed by centrifugation at 400 × *g* for 10 min. The cell pellet was washed and treated with an Fc receptor blocking agent (553142, BD Biosciences) for 15 min at room temperature. To exclude dead cells, the suspension was stained with Live/Dead Fixable Viability Stain (564996, BD Biosciences). Following the manufacturer's protocol, cells were subsequently stained with CD45 APC-Cy™7 (557659, BD Biosciences), CD31 PE-Cy™7 (561410, BD Biosciences), and EGFR PE (sc-120 PE, Santa Cruz Biotechnology) for 20 minutes at room temperature. The acquired data were processed and analyzed with FlowJo v.10.8.1 (BD Biosciences). The proportions of CD45$^-$CD31$^+$ endothelial cells and CD45$^-$CD31$^+$EGFR$^+$ endothelial cells were quantified and compared across experimental conditions.

Migration and tube formation of endothelial cells

Endothelial cells were pre-treated by three approaches: I. Pre-treatment with 0.25 μM 11,12-EET or an equal volume of complete medium for 24 h; II. Pre-treatment with the CM of shAR or shNC cell lines (e.g., MHCC97H and HCCLM3) mixed with complete medium in a 1:1 ratio for 24 h; III. Pre-treatment with the CM of MHCC97H after 48 hours of 10 nM 5α-DHT stimulation, followed by separate treatments with negative control (NC) group, 6 μM lenvatinib group (S1164, Selleck Chemicals), 10 μM gefitinib group (S1025, Selleck Chemicals) and 20 μM gefitinib group for 24 h. After the pre-treatment, the migration and tube formation assays of endothelial cells were assessed.

For migration assay, 1 × 10^4 HUVECs were seeded into the upper chamber of a transwell insert (Corning Falcon) with plain medium. The upper chamber was then placed into the transwell containing complete medium in the lower chamber. After 4–6 hours, the chambers were collected, stained with 0.5% crystal violet, and counted using ImageJ software.

For tube formation assay, 100 μL Matrigel was coated onto a 96-well plate and preincubated at 37 °C for 2 h. 1 × 10^4 HUVECs were resuspended in 200 μL of CM from MHCC97H and added to the Matrigel-coated wells. The cells were cultured at 37 °C in a 5% CO$_2$ cell culture incubator for 4–6 h. Analysis was performed using an IX83 inverted microscope (Olympus, Japan) and ImageJ software.

Establishment of HCC mouse models

All mice were maintained in a specific-pathogen-free facility. All animals received humane care in accordance with the standards outlined in the "Guidelines for the Care and Use of Laboratory Animals." Euthanasia was performed on animals when tumor size not exceeding 2000 mm^3 and overall health conditions met the euthanasia criteria. No in vivo tumors exceeded the maximal permitted tumor size.

For HCC subcutaneous mouse model, 5 × 10^6 MHCC97H (shAR/shNC, $n = 6$ for each group), 1 × 10^7 Huh7 (oeAR/oeNC, $n = 6$ for each group), 1 × 10^6 RIL-175 (shAr/shNC, $n = 6$ for each group) and 5 × 10^6 Hepa1-6 (oeAr/oeNC, $n = 6$ for each group) cells were subcutaneously injected into the right flank of six-week-old male NCG or C57BL/6 mice. Tumor growth was longitudinally monitored at designated time points until the experimental endpoint. Tumor volume was calculated using volume (cm^3) = L×W^2 × 0.5, based on previous studies[90], where L and W represent the length and width of the tumor, respectively. Statistical comparisons between treatment groups across time points were performed using two-way ANOVA. At the end of experiments, mice were sacrificed and tumors were isolated for IHC staining, ELISA and flow cytometry analysis.

3–5 × 10^6 MHCC97H cells (shAR/shNC, $n = 5$ per group) were intrahepatically injected into the liver of six-week-old male NCG mice. Following tumor establishment, mice were administered vehicle control, lenvatinib (4 mg/kg, oral gavage, once daily; S1164, Selleck Chemicals), gefitinib (80 mg/kg, oral gavage, once daily; S1025, Selleck Chemicals), bicalutamide (10 mg/kg, oral gavage, once daily; S1190, Selleck Chemicals), lenvatinib combined with bicalutamide, or gefitinib combined with bicalutamide for one week. Similarly, 3–5 × 10^6 Hepa1-6 cells (oeAr/oeNC, $n = 7$ per group) were intrahepatically injected into the liver of six-week-old male C57BL/6 mice. After tumor establishment, mice received vehicle control, lenvatinib, or lenvatinib combined with bicalutamide for one week. At the end of experiments, tumor-bearing mice were euthanized, and an abdominal surgery was performed to fully excise the liver containing the tumor. Tumor volume was then calculated using volume (cm^3) = L×W^2 × 0.5, as described in previous studies[91,92], where L and W represent the length and width of the tumor, respectively. The excised tumor tissues were then collected for subsequent experimental validations.

Statistical analysis

Statistical analysis was performed in R (v.4.2.2) or GraphPad Prism 10 (v. 10.1.0). Continuous variables were compared by Wilcoxon rank sum test for bioinformatics analysis sections and two-sided t-test for experimental validation sections, unless otherwise noted. Categorical variables were compared using chi-square test or Fisher's exact test, as appropriate. For comparisons involving multiple groups or variables, one-way ANOVA with Tukey's multiple comparisons tests and two-way ANOVA were performed, respectively. Statistical significance was defined as *p* value of less than 0.05.

Reporting summary

Further information on research design is available in the Nature Portfolio Reporting Summary linked to this article.

Data availability

The public scRNA-seq data of healthy liver samples were obtained from the Gene Expression Omnibus (GEO) Database with an accession number of GSE115469[93]. The spatial transcriptomics data were downloaded on http://lifeome.net/supp/livercancer-st/data.htm in the public dataset[94]. FPKM data and 450k DNA methylation profiles from TCGA databases were utilized, which were downloaded from UCSC Xena (https://xenabrowser.net/datapages/). Of note, we only included primary treatment-naïve HCC patients with available serum AFP levels in the TCGA Liver Cancer (TCGA-LIHC) dataset. The new datasets generated in this study could be publicly available as follows. The scRNA-seq data have been deposited in the Genome Sequence Archive (https://ngdc.cncb.ac.cn/gsa-human/) of China National Center for Bioinformation under accession code HRA008254 and HRA005769, with detailed data sources provided in Supplementary Data 4. The datasets of lipidomics, bulk RNA-seq, snATAC-seq, RRBS, and WES datasets were deposited in OMIX Database (https://ngdc.cncb.ac.cn/omix), hosted by the China National Center for Bioinformation, under accession code OMIX008233, OMIX008234, OMIX008235, OMIX008236, and OMIX008237, respectively. Datasets mentioned above are available under restricted access due to patient privacy and regulatory requirements. Researchers can request access through the Data Access Committees (DAC) of the GSA-Human and OMIX Database. The approximate response time for access requests is one month, and once approved, the data will be accessible for a duration of two months. The remaining data are available within the Article, Supplementary Information or Source Data file. Source data are provided with this paper.

References

1. Rumgay, H. et al. Global burden of primary liver cancer in 2020 and predictions to 2040. *J. Hepatol.* **77**, 1598–1606 (2022).
2. Devarbhavi, H. et al. Global burden of liver disease: 2023 update. *J. Hepatol.* **79**, 516–537 (2023).
3. Llovet, J. M. et al. Hepatocellular carcinoma. *Nat. Rev. Dis. Prim.* **7**, 6 (2021).
4. Wang, T. & Zhang, K. H. New blood biomarkers for the diagnosis of AFP-negative hepatocellular carcinoma. *Front Oncol.* **10**, 1316 (2020).
5. Zong, J., Fan, Z. & Zhang, Y. Serum tumor markers for early diagnosis of primary hepatocellular carcinoma. *J. Hepatocell. Carcinoma* **7**, 413–422 (2020).
6. Munson, P. V., Adamik, J. & Butterfield, L. H. Immunomodulatory impact of alpha-fetoprotein. *Trends Immunol.* **43**, 438–448 (2022).
7. He, H. et al. Multi-dimensional single-cell characterization revealed suppressive immune microenvironment in AFP-positive hepatocellular carcinoma. *Cell Discov.* **9**, 60 (2023).
8. Feng, L. et al. Integrated analysis of the rhesus monkey liver transcriptome during development and human primary HCC AFP-related gene expression. *Mol. Ther. Nucleic Acids* **25**, 406–415 (2021).
9. Xu, L. et al. FASN-mediated fatty acid biosynthesis remodels immune environment in Clonorchis sinensis infection-related intrahepatic cholangiocarcinoma. *J. Hepatol.* **81**, 265–277 (2024).
10. Chen, S. et al. Distinct single-cell immune ecosystems distinguish true and de novo HBV-related hepatocellular carcinoma recurrences. *Gut* **72**, 1196–1210 (2023).
11. Chi, X. et al. A comparison of clinical pathologic characteristics between alpha-fetoprotein negative and positive hepatocellular carcinoma patients from Eastern and Southern China. *BMC Gastroenterol.* **22**, 202 (2022).
12. Guo, W. et al. Circulating tumor cells with stem-like phenotypes for diagnosis, prognosis, and therapeutic response evaluation in hepatocellular carcinoma. *Clin. Cancer Res.* **24**, 2203–2213 (2018).
13. Zhu, A. X. et al. Ramucirumab versus placebo as second-line treatment in patients with advanced hepatocellular carcinoma following first-line therapy with sorafenib (REACH): a randomised, double-blind, multicentre, phase 3 trial. *Lancet Oncol.* **16**, 859–870 (2015).
14. Zhu, A. X. et al. Ramucirumab after sorafenib in patients with advanced hepatocellular carcinoma and increased alpha-fetoprotein concentrations (REACH-2): a randomised, double-blind, placebo-controlled, phase 3 trial. *Lancet Oncol.* **20**, 282–296 (2019).
15. Kudo, M. et al. Lenvatinib versus sorafenib in first-line treatment of patients with unresectable hepatocellular carcinoma: a randomised phase 3 non-inferiority trial. *Lancet* **391**, 1163–1173 (2018).
16. Khemlina, G., Ikeda, S. & Kurzrock, R. The biology of Hepatocellular carcinoma: implications for genomic and immune therapies. *Mol. Cancer* **16**, 149 (2017).
17. Ho, D. W. H. et al. TSC1/2 mutations define a molecular subset of HCC with aggressive behaviour and treatment implication. *Gut* **66**, 1496–1506 (2017).
18. Totoki, Y. et al. Trans-ancestry mutational landscape of hepatocellular carcinoma genomes. *Nat. Genet.* **46**, 1267–1273 (2014).
19. Lai, K. K. et al. Extracellular matrix dynamics in hepatocarcinogenesis: a comparative proteomics study of PDGFC transgenic and Pten null mouse models. *PLoS Genet.* **7**, e1002147 (2011).
20. Hoshida, Y. et al. Integrative transcriptome analysis reveals common molecular subclasses of human hepatocellular carcinoma. *Cancer Res.* **69**, 7385–7392 (2009).
21. Hoshida, Y. Nearest template prediction: a single-sample-based flexible class prediction with confidence assessment. *PLoS One* **5**, e15543 (2010).
22. Wu, Y. et al. Spatiotemporal immune landscape of colorectal cancer liver metastasis at single-cell level. *Cancer Discov.* **12**, 134–153 (2022).
23. Wang, B. et al. Metabolism pathways of arachidonic acids: mechanisms and potential therapeutic targets. *Signal Transduct. Target Ther.* **6**, 94 (2021).
24. Yoshinaga, K., Ishikawa, H., Beppu, F. & Gotoh, N. Incorporation of dietary arachidonic and docosatetraenoic acid into mouse brain. *J. Agric Food Chem.* **69**, 2457–2461 (2021).
25. Sprecher, H., VanRollins, M., Sun, F., Wyche, A. & Needleman, P. Dihomo-prostaglandins and -thromboxane. A prostaglandin family from adrenic acid that may be preferentially synthesized in the kidney. *J. Biol. Chem.* **257**, 3912–3918 (1982).
26. Kopf, P. G. et al. Adrenic acid metabolites as endogenous endothelium-derived and zona glomerulosa-derived hyperpolarizing factors. *Hypertension* **55**, 547–554 (2010).
27. Korbecki, J., Rebacz-Maron, E., Kupnicka, P., Chlubek, D. & Baranowska-Bosiacka, I. Synthesis and significance of arachidonic acid, a substrate for cyclooxygenases, lipoxygenases, and cytochrome P450 pathways in the tumorigenesis of glioblastoma multiforme, including a pan-cancer comparative analysis. *Cancers* **15**, 946 (2023).

28. Lambert, S. A. et al. The human transcription factors. *Cell* **172**, 650–665 (2018).
29. Aibar, S. et al. SCENIC: single-cell regulatory network inference and clustering. *Nat. Methods* **14**, 1083–1086 (2017).
30. Zhang, H., Spencer, K., Burley, S. K. & Zheng, X. F. S. Toward improving androgen receptor-targeted therapies in male-dominant hepatocellular carcinoma. *Drug Discov. Today* **26**, 1539–1546 (2021).
31. Zhang, H. et al. Significance and mechanism of androgen receptor overexpression and androgen receptor/mechanistic target of rapamycin cross-talk in hepatocellular carcinoma. *Hepatology* **67**, 2271–2286 (2018).
32. Ma, W. L. et al. Hepatic androgen receptor suppresses hepatocellular carcinoma metastasis through modulation of cell migration and anoikis. *Hepatology* **56**, 176–185 (2012).
33. Li, Y., Xu, A., Jia, S. & Huang, J. Recent advances in the molecular mechanism of sex disparity in hepatocellular carcinoma. *Oncol. Lett.* **17**, 4222–4228 (2019).
34. Pihlajamaa, P., Sahu, B. & Janne, O. A. Determinants of receptor- and tissue-specific actions in androgen signaling. *Endocr. Rev.* **36**, 357–384 (2015).
35. Rauluseviciute, I. et al. JASPAR 2024: 20th anniversary of the open-access database of transcription factor binding profiles. *Nucleic Acids Res* **52**, D174–D182 (2024).
36. Lin, J., Rao, D., Zhang, M. & Gao, Q. Metabolic reprogramming in the tumor microenvironment of liver cancer. *J. Hematol. Oncol.* **17**, 6 (2024).
37. Martinez-Reyes, I. & Chandel, N. S. Cancer metabolism: looking forward. *Nat. Rev. Cancer* **21**, 669–680 (2021).
38. Dann, E., Henderson, N. C., Teichmann, S. A., Morgan, M. D. & Marioni, J. C. Differential abundance testing on single-cell data using k-nearest neighbor graphs. *Nat. Biotechnol.* **40**, 245–253 (2022).
39. Caligiuri, G. CD31 as a therapeutic target in atherosclerosis. *Circ. Res.* **126**, 1178–1189 (2020).
40. Xu, C. et al. Single-cell transcriptomic analysis identifies an immune-prone population in erythroid precursors during human ontogenesis. *Nat. Immunol.* **23**, 1109–1120 (2022).
41. Goveia, J. et al. An integrated gene expression landscape profiling approach to identify lung tumor endothelial cell heterogeneity and angiogenic candidates. *Cancer Cell* **37**, 421 (2020).
42. Weis, S. M. & Cheresh, D. A. Tumor angiogenesis: molecular pathways and therapeutic targets. *Nat. Med* **17**, 1359–1370 (2011).
43. Zhao, Q. et al. Single-cell transcriptome analyses reveal endothelial cell heterogeneity in tumors and changes following antiangiogenic treatment. *Cancer Res.* **78**, 2370–2382 (2018).
44. Trott, O. & Olson, A. J. AutoDock Vina: improving the speed and accuracy of docking with a new scoring function, efficient optimization, and multithreading. *J. Comput. Chem.* **31**, 455–461 (2010).
45. Forli, S. et al. Computational protein-ligand docking and virtual drug screening with the AutoDock suite. *Nat. Protoc.* **11**, 905–919 (2016).
46. Kanda, T. & Yokosuka, O. The androgen receptor as an emerging target in hepatocellular carcinoma. *J. Hepatocell. Carcinoma* **2**, 91–99 (2015).
47. Galbraith, L., Leung, H. Y. & Ahmad, I. Lipid pathway deregulation in advanced prostate cancer. *Pharm. Res.* **131**, 177–184 (2018).
48. Norlin, M., Pettersson, H., Tang, W. & Wikvall, K. Androgen receptor-mediated regulation of the anti-atherogenic enzyme CYP27A1 involves the JNK/c-jun pathway. *Arch. Biochem. Biophys.* **506**, 236–241 (2011).
49. Sun, R. F. et al. Androgen receptor stimulates hexokinase 2 and induces glycolysis by PKA/CREB signaling in hepatocellular carcinoma. *Dig. Dis. Sci.* **66**, 802–813 (2021).
50. Xiao, Y. et al. Androgen receptor (AR)/miR-520f-3p/SOX9 signaling is involved in altering hepatocellular carcinoma (HCC) cell sensitivity to the Sorafenib therapy under hypoxia via increasing cancer stem cells phenotype. *Cancer Lett.* **444**, 175–187 (2019).
51. Feng, H. et al. Cell cycle-related kinase is a direct androgen receptor-regulated gene that drives beta-catenin/T cell factor-dependent hepatocarcinogenesis. *J. Clin. Investig.* **121**, 3159–3175 (2011).
52. Groupe d'Etude et de Traitement du Carcinome H. Randomized trial of leuprorelin and flutamide in male patients with hepatocellular carcinoma treated with tamoxifen. *Hepatology* **40**, 1361–1369 (2004).
53. Qin, Y. et al. Lenvatinib in hepatocellular carcinoma: resistance mechanisms and strategies for improved efficacy. *Liver Int.* **44**, 1808–1831 (2024).
54. Yang, C., Huang, X., Liu, Z., Qin, W. & Wang, C. Metabolism-associated molecular classification of hepatocellular carcinoma. *Mol. Oncol.* **14**, 896–913 (2020).
55. Li, H. & Durbin, R. Fast and accurate short read alignment with Burrows-Wheeler transform. *Bioinformatics* **25**, 1754–1760 (2009).
56. Tarasov, A., Vilella, A. J., Cuppen, E., Nijman, I. J. & Prins, P. Sambamba: fast processing of NGS alignment formats. *Bioinformatics* **31**, 2032–2034 (2015).
57. do Valle, I. F. et al. Optimized pipeline of MuTect and GATK tools to improve the detection of somatic single nucleotide polymorphisms in whole-exome sequencing data. *BMC Bioinforma.* **17**, 341 (2016).
58. Wang, K., Li, M. & Hakonarson, H. ANNOVAR: functional annotation of genetic variants from high-throughput sequencing data. *Nucleic Acids Res.* **38**, e164 (2010).
59. Lawrence, M. S. et al. Mutational heterogeneity in cancer and the search for new cancer-associated genes. *Nature* **499**, 214–218 (2013).
60. Talevich, E., Shain, A. H., Botton, T. & Bastian, B. C. CNVkit: genome-wide copy number detection and visualization from targeted DNA sequencing. *PLoS Comput. Biol.* **12**, e1004873 (2016).
61. Mermel, C. H. et al. GISTIC2.0 facilitates sensitive and confident localization of the targets of focal somatic copy-number alteration in human cancers. *Genome Biol.* **12**, R41 (2011).
62. Niu, B. et al. MSIsensor: microsatellite instability detection using paired tumor-normal sequence data. *Bioinformatics* **30**, 1015–1016 (2014).
63. Roth, A. et al. PyClone: statistical inference of clonal population structure in cancer. *Nat. Methods* **11**, 396–398 (2014).
64. Shukla, S. A. et al. Comprehensive analysis of cancer-associated somatic mutations in class I HLA genes. *Nat. Biotechnol.* **33**, 1152–1158 (2015).
65. Reynisson, B., Alvarez, B., Paul, S., Peters, B. & Nielsen, M. NetMHCpan-4.1 and NetMHCIIpan-4.0: improved predictions of MHC antigen presentation by concurrent motif deconvolution and integration of MS MHC eluted ligand data. *Nucleic Acids Res.* **48**, W449–W454 (2020).
66. Rooney, M. S., Shukla, S. A., Wu, C. J., Getz, G. & Hacohen, N. Molecular and genetic properties of tumors associated with local immune cytolytic activity. *Cell* **160**, 48–61 (2015).
67. Peng, S. et al. Combination neoantigen-based dendritic cell vaccination and adoptive T-cell transfer induces antitumor responses against recurrence of hepatocellular carcinoma. *Cancer Immunol. Res.* **10**, 728–744 (2022).
68. Islam, S. M. A. et al. Uncovering novel mutational signatures by de novo extraction with SigProfilerExtractor. *Cell Genom.* **2**, None (2022).
69. Dobin, A. et al. STAR: ultrafast universal RNA-seq aligner. *Bioinformatics* **29**, 15–21 (2013).
70. Li, B. & Dewey, C. N. RSEM: accurate transcript quantification from RNA-Seq data with or without a reference genome. *BMC Bioinforma.* **12**, 323 (2011).
71. Love, M. I., Huber, W. & Anders, S. Moderated estimation of fold change and dispersion for RNA-seq data with DESeq2. *Genome Biol.* **15**, 550 (2014).

72. Subramanian, A. et al. Gene set enrichment analysis: a knowledge-based approach for interpreting genome-wide expression profiles. *Proc. Natl. Acad. Sci. USA* **102**, 15545–15550 (2005).
73. Aran, D., Hu, Z. & Butte, A. J. xCell: digitally portraying the tissue cellular heterogeneity landscape. *Genome Biol.* **18**, 220 (2017).
74. Guo, W. et al. Notch signaling regulates macrophage-mediated inflammation in metabolic dysfunction-associated steatotic liver disease. *Immunity* **57**, 2310–2327.e2316 (2024).
75. Wu, Y. et al. Neutrophil profiling illuminates anti-tumor antigen-presenting potency. *Cell* **187**, 1422–1439.e1424 (2024).
76. Zhang, L. et al. Single-cell analyses inform mechanisms of myeloid-targeted therapies in colon cancer. *Cell* **181**, 442–459.e429 (2020).
77. Krueger, F. & Andrews, S. R. Bismark: a flexible aligner and methylation caller for Bisulfite-Seq applications. *Bioinformatics* **27**, 1571–1572 (2011).
78. Young M. D., Behjati S. SoupX removes ambient RNA contamination from droplet-based single-cell RNA sequencing data. *Gigascience* **9**, giaa151 (2020).
79. Hao, Y. et al. Integrated analysis of multimodal single-cell data. *Cell* **184**, 3573–3587.e3529 (2021).
80. Korsunsky, I. et al. Fast, sensitive and accurate integration of single-cell data with Harmony. *Nat. Methods* **16**, 1289–1296 (2019).
81. Wu, T. et al. clusterProfiler 4.0: a universal enrichment tool for interpreting omics data. *Innovative* **2**, 100141 (2021).
82. Jassal, B. et al. The reactome pathway knowledgebase. *Nucleic Acids Res.* **48**, D498–D503 (2020).
83. Hanzelmann, S., Castelo, R. & Guinney, J. GSVA: gene set variation analysis for microarray and RNA-seq data. *BMC Bioinforma.* **14**, 7 (2013).
84. Van de Sande, B. et al. A scalable SCENIC workflow for single-cell gene regulatory network analysis. *Nat. Protoc.* **15**, 2247–2276 (2020).
85. Suo, S. et al. Revealing the critical regulators of cell identity in the mouse cell atlas. *Cell Rep.* **25**, 1436–1445.e1433 (2018).
86. Mercatelli, D., Lopez-Garcia, G. & Giorgi, F. M. corto: a lightweight R package for gene network inference and master regulator analysis. *Bioinformatics* **36**, 3916–3917 (2020).
87. Stuart, T., Srivastava, A., Madad, S., Lareau, C. A. & Satija, R. Single-cell chromatin state analysis with Signac. *Nat. Methods* **18**, 1333–1341 (2021).
88. Granja, J. M. et al. ArchR is a scalable software package for integrative single-cell chromatin accessibility analysis. *Nat. Genet.* **53**, 403–411 (2021).
89. O'Boyle, N. M. et al. Open Babel: an open chemical toolbox. *J. Cheminform.* **3**, 33 (2011).
90. Tomayko, M. M. & Reynolds, C. P. Determination of subcutaneous tumor size in athymic (nude) mice. *Cancer Chemother. Pharm.* **24**, 148–154 (1989).
91. Carlsson, G. & Gullberg, B. Hafstrom L. Estimation of liver tumor volume using different formulas—an experimental study in rats. *J. Cancer Res. Clin. Oncol.* **105**, 20–23 (1983).
92. Kasashima, H. et al. An orthotopic implantation mouse model of hepatocellular carcinoma with underlying liver steatosis. *STAR Protoc.* **1**, 100185 (2020).
93. MacParland, S. A. et al. Single cell RNA sequencing of human liver reveals distinct intrahepatic macrophage populations. *Nat. Commun.* **9**, 4383 (2018).
94. Wu, R. et al. Comprehensive analysis of spatial architecture in primary liver cancer. *Sci. Adv.* **7**, eabg3750 (2021).

Acknowledgements

We gratefully acknowledge the joint support of the National Natural Science Foundation of China (grant number 82172047, 82373004), the Key Research and Development Plan of Guangzhou City (grant number 202206080016), the Research and Development Plan for Key Areas in Guangdong Province (grant number 2023B1111020007) and National Science Fund for Distinguished Young Scholars (grant number 82322034).

Author contributions

Z.D. was responsible for the overall content as the guarantor. Z.D., Z.P. and S.P. conceived and supervised this study. Z.L., X.L., H.W., S.L., Z.M., J.Y., Y.Z., K.L., Y.W., Y.K., R.Z., Z.X., Y.W. and X.R. performed sample preparation, experimental operation and data generation. C.L., A.S.C., Y.X., S.C. and M.K. commented on the study and revised the manuscript. Z.L., X.L. and H.W. performed bioinformatics analyses. Z.L. wrote the manuscript.

Competing interests

The authors declare no competing interests.

Additional information

Supplementary information The online version contains supplementary material available at https://doi.org/10.1038/s41467-025-61448-z.

Correspondence and requests for materials should be addressed to Sui Peng, Zhenwei Peng or Zihao Dai.

Peer review information *Nature Communications* thanks Timothy Humpton, Nikolaos Trasanidis, Youqiong Ye and the other anonymous reviewer(s) for their contribution to the peer review of this work. A peer review file is available.